General relativistic force-free electrodynamics with a discontinuous Galerkin-finite difference hybrid method

Yoonsoo Kim,[1,*] Elias R. Most,[1,2] William Throwe,[3] Saul A. Teukolsky,[1,2,3] and Nils Deppe[4,3]

[1]*Theoretical Astrophysics 350-17, California Institute of Technology, Pasadena, California 91125, USA*
[2]*Walter Burke Institute for Theoretical Physics, California Institute of Technology, Pasadena, California 91125, USA*
[3]*Cornell Center for Astrophysics and Planetary Science, Cornell University, Ithaca, New York 14853, USA*
[4]*Department of Physics, Cornell University, Ithaca, New York 14853, USA*

(Received 1 April 2024; accepted 14 May 2024; published 10 June 2024)

Relativistic plasmas around compact objects can sometimes be approximated as being force-free. In this limit, the plasma inertia is negligible and the overall dynamics is governed by global electric currents. We present a novel numerical approach for simulating such force-free plasmas, which allows for high accuracy in smooth regions as well as capturing dissipation in current sheets. Using a high-order accurate discontinuous Galerkin method augmented with a conservative finite-difference method, we demonstrate efficient global simulations of black hole and neutron star magnetospheres. In addition to a series of challenging test problems, we show that our approach can—depending on the physical properties of the system and the numerical implementation—be up to 10× more efficient than conventional simulations, with a speedup of 2–3× for most problems we consider in practice.

DOI: 10.1103/PhysRevD.109.123019

I. INTRODUCTION

Compact objects such as neutron stars and black holes can feature some of the strongest magnetic fields in the Universe. Under these conditions, the environments surrounding them can be filled with a highly conducting plasma. The plasma dynamics of these magnetospheres are thought to be responsible for several observable transients in the radio [1–3] and x-ray [4–8] bands. While the description of emission processes fundamentally necessitates modeling the relevant kinetic scales [9,10], the available energy budget as well as the presence of any dissipative or emitting region inside the magnetosphere is a result of the bulk dynamics. It is this latter aspect that our present work aims to advance. Since these scenarios are highly nonlinear, their effective description requires numerical approaches.

The global dynamics of the plasma is usually modeled under several simplifying assumptions. In a very strongly magnetized magnetosphere, the inertia of the plasma can approximately be neglected [11,12]. In this force-free electrodynamics (FFE) state, the evolution of the system is governed largely by bulk currents, obtained via an effective closure of the Maxwell equations. It is important to point out that the main assumption—neglecting plasma inertia—can break down, e.g., during shock formation, as well as the absence of physically meaningful dissipation in reconnection regions. In this regime, the closest extension of force-free electrodynamics is magnetohydrodynamical (MHD) models, retaining a single-component plasma rest-mass density. MHD studies of relativistic magnetospheres are not commonly employed (see, e.g., Ref. [13] for a notable exception in neutron star magnetospheres). Instead, most studies adopt an FFE approach.

Recent examples include applications to magnetar quakes [14], nonlinear steepening of Alfvén waves [15,16], magnetar giant flares [17–20], outbursts from gravitational collapse of a neutron star [21] (see also Refs. [22,23] for related studies in electrovacuum), and black hole and neutron star magnetospheres [24–28]. Apart from isolated compact objects, force-free electrodynamics has also been employed in the context of jets from massive black hole mergers [29,30] and potential electromagnetic precursor to gravitational wave events involving merger of compact objects [31–37].

Several approaches have been adopted in the literature for numerically solving the FFE equations. Most commonly, either unlimited finite-difference [25,27,29,38,39] or conservative finite-volume schemes [34,40–46] have been employed. These methods are robust, can easily capture strong gradients inside the magnetosphere, and work well with commonly employed mesh refinement techniques [47]. However, they come with a major drawback. Properly capturing wave solutions over long integration times, e.g., Alfvén waves [15], requires a large number of grid points, especially when less accurate

*Corresponding author: ykim7@caltech.edu

versions of finite-difference/volume schemes are being used. This prohibitively increases computational costs, especially for applications such as compact binary magnetospheres in which scale separations can span two orders of magnitude.

On the other hand, spectral-type methods such as the pseudospectral method offer exponential convergence for smooth solutions, providing a maximum in accuracy over computational cost. Several studies have made use of spectral schemes to solve the FFE equations [48–50]. One serious limitation of spectral methods is the appearance of unphysical oscillations (Gibbs phenomenon) near a discontinuity or a large gradient e.g. current sheets, which are naturally present in compact object magnetospheres. Remedying these numerical instabilities requires special treatments such as filtering or a limiting procedure [51]. In addition, globally spectral methods are not easily parallelizable, making it difficult to simulate physical scenarios with large scale separations.

To counteract this shortcoming, popular approaches in the literature focus on spectral element methods in which the computational domain is divided into nonoverlapping spectral elements, communicating only with the directly neighboring elements through the element boundaries. This approach allows for highly parallelizable implementations while retaining the exponential convergence property for smooth solutions. A concrete example of this approach, a discontinuous Galerkin (DG) method, is gaining its popularity in computational fluid dynamics and astrophysics [e.g. [52–61]], as well as in FFE [62,63].

While a DG scheme naturally permits a discontinuity at the element boundary, without special care to suppress unphysical oscillations, it suffers from the same fate as globally spectral methods described above. Several strategies have been proposed in the DG literature, which are frequently referred to as *limiters*. Common types of DG limiters are implemented as direct manipulations on spectral coefficients, addition of artificial viscosity, or a flattening correction of the solution with respect to its average value within an element. We refer the reader to [53,64] and references therein for the available types of DG limiters and related discussions.

DG limiters currently are not particularly accurate or reliable compared with corresponding finite-volume or finite-difference techniques, especially for curved meshes or relativistic applications (see, e.g., Ref. [64]). A recently developed alternative strategy is to supplement the DG evolution with a more robust subelement discretization, which has been mostly chosen to be finite volume [e.g. [53–55,65–69]]. Motivated by the idea of the *a posteriori* finite-volume limiting approach of Ref. [65], the discontinuous Galerkin-finite difference (DG-FD) hybrid method was introduced by [64] (see also Refs. [58,70] for applications to relativistic fluid dynamics simulations).

In this paper, we present a new numerical scheme and code for general-relativistic FFE simulations based on a discontinuous Galerkin discretization. Our motivation is twofold. First, we explore the suitability of the DG-FD hybrid approach to enable large-scale, parallel yet accurate numerical simulations, especially of compact binary magnetospheres. Second, since FFE on physical grounds has very localized regions of nonsmoothness such as current sheets, these simulations serve as an ideal testbed to calibrate and assess the usefulness of the DG-FD hybrid approach. Our hybrid scheme also incorporates previously developed implicit-explicit time integration schemes [71] (see Refs. [34,35] for applications to the FFE system), which allows us to enforce a set of algebraic constraints present in the FFE system. This joint approach achieves high-order convergence in smooth regions while capturing discontinuous features such as magnetic reconnection points and current sheets.

This article is organized as follows. In Sec. II, we briefly review Maxwell's equations in general relativity and introduce the formulation we adopt in this work. We also discuss our strategy for maintaining the force-free conditions in simulations. In Sec. III, we describe the numerical implementation of spatial discretization, time stepping, and the discontinuous Galerkin-finite difference hybrid solver. We present results from a set of test problems in Sec. IV, and conclude with a discussion of result in Sec. V.

In this paper, we adopt geometrized ($c = G = 1$) Heaviside-Lorentz units, where electric and magnetic fields have been rescaled by $1/\sqrt{4\pi}$ compared to Gaussian units. We use the abstract index notation using latin indices $(a, b, \cdots)$ for spacetime tensors, but reserve $\{i, j, k, \ldots\}$ for spatial tensors. We follow the sign convention of the Levi-Civita tensor from [72], $\varepsilon_{abcd} = \sqrt{-g}[abcd]$, where g is the determinant of spacetime metric and $[abcd] = \pm 1$ with $[0123] = +1$ is the flat-space antisymmetric symbol.[1]

II. GENERAL RELATIVISTIC FORCE-FREE ELECTRODYNAMICS

We begin by outlining the mathematical description used to numerically study magnetospheric dynamics. This includes a general relativistic formulation of electrodynamics in a curved spacetime, which is then specialized to the force-free case: general relativistic force-free electrodynamics (GRFFE).

A. Electrodynamics

The dynamics of electric and magnetic fields is governed by the Maxwell equations. In covariant form, they are given by

$$\nabla_b F^{ab} = \mathcal{J}^a \tag{1}$$

[1]Note that an opposite sign convention is sometimes adopted in the literature [e.g., [32,73]].

$$\nabla_b {}^*F^{ab} = 0 \tag{2}$$

where F^{ab} and ${}^*F^{ab} = \varepsilon^{abcd}F_{cd}/2$ are the electromagnetic field tensor and its dual, and $\mathcal{J}^a$ is the electric 4-current density.

For the standard $3+1$ decomposition of the spacetime metric

$$ds^2 = -\alpha^2 dt^2 + \gamma_{ij}(dx^i + \beta^i dt)(dx^j + \beta^j dt), \tag{3}$$

where α is lapse, β^i is the shift vector, and γ_{ij} is the spatial metric, the normal to spatial hypersurfaces is given by

$$n^a = (1/\alpha, -\beta^i/\alpha), \qquad n_a = (-\alpha, 0). \tag{4}$$

In terms of the normal vector n^a, electromagnetic field tensor F^{ab} and its dual ${}^*F^{ab}$ can be decomposed as

$$F^{ab} = n^a E^b - n^b E^a - \varepsilon^{abcd} B_c n_d, \tag{5}$$

$${}^*F^{ab} = -n^a B^b + n^b B^a - \varepsilon^{abcd} E_c n_d, \tag{6}$$

where

$$n_a E^a = n_a B^a = 0. \tag{7}$$

$E^a = (0, E^i)$ and $B^a = (0, B^i)$ are electric and magnetic fields in the frame of an Eulerian observer. One can read off E^a and B^a from F^{ab} using the following relations

$$E^a = F^{ab} n_b, \tag{8}$$

$$B^a = -\frac{1}{2}\varepsilon^{abcd} n_b F_{cd} = -{}^*F^{ab} n_b. \tag{9}$$

While analytically complete, Maxwell equations cannot be directly evolved numerically, as any violation of the divergence constraints [Eqs. (1) and (2) with $a = 0$] will break strong hyperbolicity of the system [74,75]. This can be avoided by either using constrained transport approaches [76] or extending the system using effective Lagrange multipliers [77]. We here adopt the latter approach. The extended (or augmented) Maxwell equations [73,78] are

$$\nabla_a (F^{ab} + g^{ab}\psi) = -\mathcal{J}^b + \kappa_\psi n^b \psi \tag{10}$$

$$\nabla_a ({}^*F^{ab} + g^{ab}\phi) = \kappa_\phi n^b \phi \tag{11}$$

$$\nabla_a \mathcal{J}^a = 0 \tag{12}$$

where auxiliary scalar fields ψ and ϕ propagate divergence constraint violations of electric field and magnetic field. κ_ψ and κ_ϕ are damping constants, leading to an exponential damping of the constraints in the characteristic timescales $\kappa^{-1}_{\psi,\phi}$.

Performing a standard $3+1$ decomposition of the extended Maxwell's equations (10)–(12) using the normal vector n^a and the spatial projection operator ${h^a}_b \equiv {\delta^a}_b + n^a n_b$, we get

$$(\partial_t - \mathcal{L}_\beta)E^i - \varepsilon^{ijk}_{(3)} D_j(\alpha B_k) + \alpha\gamma^{ij} D_j \psi = -\alpha J^i + \alpha K E^i, \tag{13a}$$

$$(\partial_t - \mathcal{L}_\beta)B^i + \varepsilon^{ijk}_{(3)} D_j(\alpha E_k) + \alpha\gamma^{ij} D_j \phi = \alpha K B^i, \tag{13b}$$

$$(\partial_t - \mathcal{L}_\beta)\psi + \alpha D_i E^i = -\alpha\kappa_\psi \psi + \alpha q, \tag{13c}$$

$$(\partial_t - \mathcal{L}_\beta)\phi + \alpha D_i B^i = -\alpha\kappa_\phi \phi, \tag{13d}$$

$$(\partial_t - \mathcal{L}_\beta)q + D_i(\alpha J^i) = \alpha q K, \tag{13e}$$

where $D_i = {h^a}_i \nabla_a$ is the spatial covariant derivative, K is the trace of extrinsic curvature, $q = -n_\mu \mathcal{J}^\mu$ is the electric charge density measured by an Eulerian observer, and $J^i = {h^i}_a \mathcal{J}^a$ is the spatial electric current density. Here we also defined the spatial Levi-Civita tensor associated with the spatial metric as

$$\varepsilon^{abc}_{(3)} \equiv n_d \varepsilon^{dabc}. \tag{14}$$

The Lie derivative along the shift vector applied to a spatial vector E^i is

$$\mathcal{L}_\beta E^i = \beta^j \partial_j E^i - E^j \partial_j \beta^i,$$

and same for B^i on the left-hand side of Eq. (13), while it is simply a directional derivative (e.g. $\mathcal{L}_\beta(q) = \beta^i \partial_i q$) when applied to a scalar variable.

Evolution equations (13) can be cast into conservative form

$$\partial_t \mathbf{U} + \partial_j \mathbf{F}^j = \mathbf{S}, \tag{15}$$

with evolved variables

$$\mathbf{U} = \sqrt{\gamma}\begin{bmatrix} E^i \\ B^i \\ \psi \\ \phi \\ q \end{bmatrix} \equiv \begin{bmatrix} \tilde{E}^i \\ \tilde{B}^i \\ \tilde{\psi} \\ \tilde{\phi} \\ \tilde{q} \end{bmatrix}, \tag{16}$$

fluxes

$$\mathbf{F}^j = \begin{bmatrix} -\beta^j \tilde{E}^i + \alpha(\gamma^{ij}\tilde{\psi} - \varepsilon^{ijk}_{(3)}\tilde{B}_k) \\ -\beta^j \tilde{B}^i + \alpha(\gamma^{ij}\tilde{\phi} + \varepsilon^{ijk}_{(3)}\tilde{E}_k) \\ -\beta^j\tilde{\psi} + \alpha\tilde{E}^j \\ -\beta^j\tilde{\phi} + \alpha\tilde{B}^j \\ \tilde{J}^j - \beta^j\tilde{q} \end{bmatrix}, \tag{17}$$

and source terms

$$\mathbf{S} = \begin{bmatrix} -\alpha\sqrt{\gamma}J^i - \tilde{E}^j\partial_j\beta^i + \tilde{\psi}(\gamma^{ij}\partial_j\alpha - \alpha\gamma^{jk}\Gamma^i_{jk}) \\ -\tilde{B}^j\partial_j\beta^i + \tilde{\phi}(\gamma^{ij}\partial_j\alpha - \alpha\gamma^{jk}\Gamma^i_{jk}) \\ \tilde{E}^k\partial_k\alpha + \alpha\tilde{q} - \alpha\tilde{\psi}(K + \kappa_\psi) \\ \tilde{B}^k\partial_k\alpha - \alpha\tilde{\phi}(K + \kappa_\phi) \\ 0 \end{bmatrix}, \tag{18}$$

where Γ^i_{jk} are the Christoffel symbols associated with the spatial metric. A prescription for the electric current density J^i (Ohm's law) needs to be supplied to close the system.

B. Force-free limit

In the magnetospheres of neutron stars and black holes, we expect copious production of electron-positron pairs [79]. The resulting plasma will be highly conductive, effectively screening electric field components parallel to the magnetic field. In addition, the magnetization of the plasma will be very high, allowing us to consider the limit in which the Lorentz force density vanishes and the plasma becomes force-free.

The force-free conditions are given as

$$F^{ab}\mathcal{J}_b = 0, \tag{19}$$

$${}^*F^{ab}F_{ab} = 0, \tag{20}$$

$$F^{ab}F_{ab} > 0. \tag{21}$$

In terms of E^i, B^i, q and J^i, these conditions are

$$qE^i + \varepsilon^{ijk}_{(3)}J_jB_k = 0, \tag{22}$$

$$E^aB_a = E^iB_i = 0, \tag{23}$$

$$B^2 - E^2 > 0, \tag{24}$$

where $E^2 = E_aE^a = E_iE^i$ and $B^2 = B_aB^a = B_iB^i$. The first condition (22) corresponds to the vanishing Lorentz force density, and the second one (23) shows the screening of electric field along magnetic field lines. The third condition (24) is called magnetic dominance, and violation of this constraint flags the breakdown of force-free electrodynamics; characteristic speeds associated with Alfvén modes become complex and Maxwell equations are no longer hyperbolic [80]. Physically, $E^2 \approx B^2$ means that the plasma drift speed approaches the speed of light, beyond which the FFE approximation breaks down.

The force-free conditions also give constraints on the electric current density. Equation (22) gives J^i in the form

$$J^i = q\frac{\varepsilon^{ijk}_{(3)}E_jB_k}{B^2} + \frac{(J_lB^l)}{B^2}B^i, \tag{25}$$

which leaves the parallel component J_lB^l undetermined. The first term on the right hand side of (25), the drift current, is perpendicular to both electric and magnetic fields and shows that electric charge moves collectively with the drift velocity $v_d = \varepsilon^{ijk}_{(3)}E_jB_k/B^2$.

Requiring Eq. (23) to always be satisfied, we obtain a closed form expression of the parallel current J_lB^l as [43,81]

$$J_lB^l = \epsilon^{ijk}_{(3)}(B_iD_jB_k - E_iD_jE_k) - 2E^iB^jK_{ij}, \tag{26}$$

which reduces to

$$J_lB^l = B_i(\nabla \times B)^i - E_j(\nabla \times E)^j \tag{27}$$

in the special relativistic limit [12].

The parallel current Eq. (26) contains the spatial derivatives of E and B, the dynamical variables that we evolve. Including these derivatives in the source terms changes the principal part of the Maxwell PDE system, and the resulting system of equations is not strongly hyperbolic [80].

A straightforward way to keep the force-free conditions satisfied in numerical simulations is to algebraically impose Eqs. (23) and (24) in the time evolution [25,27,29,46,48–50]. This commonly employed approach exactly ensures the force-free conditions, but reduces the numerical accuracy to first-order convergence in time.

As we aim to implement a higher-order numerical scheme for GRFFE, we consider an alternative strategy. We adopt the driver term approach first implemented in [31,82] and applied in later studies [e.g. [34,35]]. In this method, a stiff relaxation term is added to the electric current density J^i to continuously damp the violation of the force-free conditions. We adopt the following electric current density prescription [35]

$$J^i = q\frac{\varepsilon^{ijk}_{(3)}E_jB_k}{B^2} + \eta\left[\frac{E_jB^j}{B^2}B^i + \frac{\mathcal{R}(E^2 - B^2)}{B^2}E^i\right], \tag{28}$$

where $\mathcal{R}(x) \equiv \max(x, 0)$ is the rectifier function and η is a relaxation parameter. The parallel current consists of the terms in the square bracket in Eq. (28), each being proportional to the violation of the force-free conditions (23) and (24). They are coupled to the evolution of electric field and drive the solution to the force-free limit with the

characteristic damping timescale η^{-1}. The limiting case $\eta \to \infty$ corresponds to the ideal force-free limit.

A caveat to the FFE simulations with a parallel electric current is that the energy loss from an Ohmic dissipation $J_i E^i$ is removed out from and no further tracked in simulations; therefore, total electromagnetic energy is not conserved.[2] While numerical dissipation will also contribute to the energy loss, the amount of energy dissipation in current sheets [corresponding to the rectifier term in Eq. (28)] dominates, albeit likely at a different rate compared to a full kinetic reconnection model [e.g. [9,83]].

III. NUMERICAL IMPLEMENTATION

In this section, we describe the details of our numerical scheme and its implementation. We present our method of spatial discretization in Sec. III A, time integration in Sec. III B, and the adaptive discontinuous Galerkin-finite difference hybrid solver in Sec. III C. Our numerical scheme described here is implemented in the open source numerical relativity code SpECTRE [84].

A. Domain decomposition and spatial discretization

The computational domain typically used in astrophysics or numerical relativity simulations is simple enough to be decomposed into a set of nonoverlapping deformed cubes. We divide the domain into these deformed cubes, which are called subdomain elements (hereafter simply *elements*). Neighboring elements share their boundaries at an element interface between them.

Within each element, a spectral expansion can be performed to represent a field of interest. We also need to define a prescription for handling boundary corrections from element interfaces. This family of numerical methods is broadly called spectral element methods [85]. We choose to adopt the nodal discontinuous Galerkin discretization [51], so our approach is formally referred to as a discontinuous Galerkin spectral element method (DG-SEM), which is often simply called a discontinuous Galerkin (DG) method.

Each element is mapped to a reference cube spanning $\{\xi^1, \xi^2, \xi^3\} \in [-1, 1]^3$ in the reference coordinate system $\{\xi^i\}$. A coordinate map $x^i(\xi^j)$ relates the reference coordinates ξ^j to physical coordinates x^i. A set of collocation points $\{\xi^1_i, \xi^2_j, \xi^3_k\}$ are chosen to represent the solution

$$u(\xi) = \sum_{i,j,k} u_{i,j,k} \phi_{i,j,k}(\xi) \tag{29}$$

where $u_{i,j,k} = u(\xi^1_i, \xi^2_j, \xi^3_k)$ is the value of the solution at the collocation point $(\xi^1_i, \xi^2_j, \xi^3_k)$, and $\phi_{i,j,k}(\xi)$ is the nodal basis function

$$\phi_{i,j,k}(\xi^1_l, \xi^2_m, \xi^3_n) = \left\{ \begin{array}{ll} 1, & \text{for } i = l, j = m, k = n \\ 0, & \text{otherwise} \end{array} \right\}. \tag{30}$$

We use the tensor product basis

$$\phi_{i,j,k}(\xi) = l_i(\xi^1) l_j(\xi^2) l_k(\xi^3) \tag{31}$$

where $l_d(x)$ is the 1D Lagrange polynomial interpolating collocation points along the dth axis. We choose to use an isotropic DG mesh with the same polynomial degree N for each spatial dimension. The resulting nodal expansion of the solution is

$$u(\xi) = \sum_{i=0}^{N} \sum_{j=0}^{N} \sum_{k=0}^{N} u_{i,j,k} l_i(\xi^1) l_j(\xi^2) l_k(\xi^3). \tag{32}$$

The solution (32) can be also represented in a modal form

$$u(\xi) = \sum_{p=0}^{N} \sum_{q=0}^{N} \sum_{r=0}^{N} c_{p,q,r} L_p(\xi^1) L_q(\xi^2) L_r(\xi^3), \tag{33}$$

where $L_p(x)$ is the Legendre polynomial of degree p. See also Ref. [86] for a detailed derivation of formulating the DG scheme in a curved spacetime.

In this article, we denote a scheme using the Nth degree polynomial basis (i.e. $N + 1$ collocation points) in each spatial dimension as a DG-P_N scheme. For instance, a DG-P_5 scheme uses 6^3 collocation points in each element and a solution is approximated as a fifth degree polynomial in each spatial direction. When the solution is smooth, a DG-P_N scheme exhibits $\mathcal{O}(L^{N+1})$ spatial convergence where L is the spatial size of an element.

We mainly use a DG-P_5 scheme, although we present results for different DG orders where necessary. We use the Legendre-Gauss-Lobatto collocation points with the mass lumping approximation [87]. For a reduced aliasing error, an exponential filter is applied to rescale the modal coefficients $c_{p,q,r}$ in Eq. (33):

$$c_{p,q,r} \to c_{p,q,r} \prod_{n=\{p,q,r\}} \exp\left[-a\left(\frac{n}{N}\right)^{2b}\right] \tag{34}$$

after every DG time (sub)step. We use $a = 36$ and $b = 50$, which effectively zeros only the highest mode ($i = N$) and leaves other modes intact.[3] Filtering out the highest mode reduces expected spatial converge of a DG-P_N scheme from $\mathcal{O}(L^{N+1})$ to $\mathcal{O}(L^N)$.

[2] In a MHD model, it is captured as the same amount of increase in the internal (thermal) energy of the plasma.

[3] We note that this is a common practice adopted in spectral methods for curing aliasing and has marginal effects on capturing discontinuities, since typically a Gibbs phenomenon near a discontinuity excites not only the highest mode but multiple high modes simultaneously.

B. Time integration

Based on the spatial discretization presented in the previous section, evolution equations can be integrated over time using the method of lines.

The maximum admissible time step size for a DG-P_N scheme is [65,88]

$$\Delta t \leq \frac{L}{\lambda_{\max}(2N+1)}\frac{c}{D} \tag{35}$$

where L is the minimum (Cartesian) edge length of an element, $\lambda_{\max}$ is the maximum characteristic speed inside the element, c is a stability constant specific to a time stepper, which is usually of order unity,[4] and D is the number of spatial dimensions.

However, usage of a nontrivial coordinate map $x(\xi)$ and a complex geometry of elements deforms the spatial distribution of grid points, and an actual upper bound can differ from Eq. (35). As a practical strategy, we adopt the following expression

$$\Delta t = f\frac{(\Delta x)_{\min}}{\lambda_{\max}}\frac{c}{D} \tag{36}$$

for the DG time step size, where $(\Delta x)_{\min}$ is the minimum grid spacing between DG collocation points in physical coordinates and f is the CFL factor.

In order to keep the force-free constraint violations as small as possible during evolution, we aim to use a large value of the damping coefficient η for the driver term in Eq. (28), possibly up to $\eta\Delta t \gtrsim 10$. This implies that the characteristic timescale of constraint damping η^{-1} is smaller than the time step size, which introduces stiffness in evolution equations and makes explicit time integration unstable unless an unreasonably small time step is used.

To address the stiffness from rapid constraint damping, we adopt the implicit-explicit (IMEX) time stepping technique. In particular, we make use of the IMEX-SSP3(4,3,3) scheme [71], which is third order in time. In this IMEX approach, we evolve all quantities explicitly using a standard 3rd-order Runge-Kutta scheme, and treat only the stiff part of the source terms (18) implicitly. Specifically, in the evolution of electric fields this requires us to solve the following nonlinear algebraic equation at all substeps,

$$E^i = (E^i)^* - \alpha\eta\Delta t'\left[\frac{E_j B^j}{B^2}B^i + \frac{\mathcal{R}(E^2-B^2)}{B^2}E^i\right] \tag{37}$$

where $(E^i)^*$ are provided values and $\Delta t'$ is an IMEX-scheme-dependent corrector step size. When $E^2 < B^2$, the solution to this equation is analytical whereas in general cases we employ a three-dimensional Newton-Raphson solver with a specific initial guess.

In addition to the stiff electric current, we also apply the IMEX time integration to the hyperbolic divergence cleaning parts to ensure stability,

$$\psi = \psi^* - \kappa_\psi\Delta t'\psi, \tag{38}$$

$$\phi = \phi^* - \kappa_\phi\Delta t'\phi, \tag{39}$$

which are linear equations and have exact analytic inversions.

Because of the simplicity of the implicit equations in our evolution system, the cost overhead from using an IMEX scheme is less than 5% of the total runtime. Being able to use much larger time steps more than compensates for this.

C. The discontinuous Galerkin-finite difference hybrid method

This section describes our implementation of the DG-FD hybrid solver for GRFFE equations. We closely follow the original implementation of [64], which was designed for GRMHD, with several improvements and adaptations.

1. Overview of the algorithm

Consider an element performing a time step on the DG grid. After each substep of the time integrator, the candidate solution is monitored by the *troubled cell indicator* (TCI) to check if the solution is admissible on the DG grid. If it is admissible, we continue with the updated solution on the DG grid. If the candidate solution is inadmissible, the troubled cell indicator is flagged, we undo the DG substep, project the DG solution onto the subelement FD grid, then repeat the substep using the FD solver. Evolution on the FD grid proceeds in a similar way; after every time step the solution gets monitored by the troubled cell indicator, which determines whether the solution needs to stay on the FD grid or it is admissible on the DG grid. If the candidate solution looks admissible on the DG grid, the solution is projected back to the DG grid and the evolution proceeds using the DG solver.

An optimal number of subelement finite-difference grid points for a DG-P_N scheme is $2N+1$ [65]. We follow such a prescription, and an element with $(N+1)^D$ collocation points on the DG grid is switched to $(2N+1)^D$ FD cells with a uniform grid spacing $\Delta\xi^i = 2/(2N+1)$ in the reference coordinates.

At the code initialization phase, all physical quantities are evaluated on the FD grid to avoid potential spurious oscillations arising from a spectral representation of the initial data. Next, each element projects evolved variables onto the DG grid, then either switches to the DG grid or stays on the FD grid depending on the decision made by the troubled cell indicator.

[4]For example, the classic 4th-order Runge-Kutta method has $c \approx 1.39$ [89].

The projection algorithm of scalar and tensor quantities between DG and FD grids is described in detail in [64]. We use a general sixth-order accurate interpolation scheme. Since the scheme is general and does not respect the physical constraints,[5] repeated applications (i.e., switching back and forth between DG and FD too frequently) can introduce spurious errors in the solution. To suppress this behavior, we design the troubled cell indicator to apply tighter criteria when switching back from FD to DG grid; see Sec. III C 3.

2. Finite difference solver

Evolution on the finite-difference grid is performed using a conservative finite-difference scheme [90,91]. For an element using a DG-P_N scheme, we divide the reference coordinate interval $[-1,1]$ into $2N+1$ finite-difference cells and project a solution from the DG grid onto cell-centered values $\{U_{\hat{i}}\}$. A flux-balanced law (15) is discretized as

$$\frac{dU_{\hat{i}}}{dt}+\left(\frac{\partial\xi^k}{\partial x^j}\right)\frac{\hat{F}^j_{\hat{i}+1/2}-\hat{F}^j_{\hat{i}-1/2}}{\Delta\xi^k}=S(U_{\hat{i}}) \tag{40}$$

where we used hat indices to label FD cells and plain indices to label spatial directions.

Computation of a numerical flux $\hat{F}^j_{\hat{i}+1/2}$ is dimensionally split, and closely follows that of the ECHO scheme [92] (see also Ref. [93] for an application to neutron star mergers). At the left and right sides of the FD cell interface $x_{\hat{i}+1/2}$, evolved variables are reconstructed using their cell-centered values $\{U_{\hat{i}}\}$. In our implementation, densitized electric current density $\tilde{J}^i$ is also reconstructed to compute fluxes associated with $\tilde{q}$ (see also Ref. [73]).

Once face-centered values $U^{L,R}_{\hat{i}+1/2}$ are reconstructed, the interface Riemann flux $F^*_{\hat{i}+1/2}$ is computed using the Rusanov (local-Lax-Friedrichs) flux formula [94]. Since the principal part of our equations is linear, this solver will reduce to the exact solution (see Ref. [77]).

In order to achieve high-order accuracy, a high-order derivative corrector is added to the interface Riemann flux to obtain the final numerical flux:

$$\hat{F}_{\hat{i}+1/2}=F^*_{\hat{i}+1/2}-G^{(4)}_{\hat{i}+1/2}. \tag{41}$$

The original ECHO scheme uses the Riemann fluxes from cell interfaces (e.g. $F^*_{\hat{i}\pm3/2}$) for the higher-order correction term $G^{(4)}_{\hat{i}+1/2}$. Since we do not employ a constrained-transport algorithm requiring a consistent and fixed stencil, we opt for simpler cell-centered fluxes (e.g., $F_{\hat{i}\pm1}$) for a more compact stencil and reduced amount of data communications (see Refs. [95,96]).

For the simulations presented in this work, we use the WENO5-Z reconstruction with the nonlinear weight exponent $q=2$ [97]. The high-order finite-difference corrector is currently implemented only on Cartesian meshes. We therefore use it for all of our one-dimensional test problems, where we assess numerical convergence of the scheme, and defer to future work its applications in multi-dimensional contexts. Consistent with previous assessments, we find it sufficient to use only a fourth-order accurate derivative correction when combined with WENO5-Z [93].

3. Troubled cell indicator

In order to decide when to switch between DG and FD grids, our numerical scheme requires a robust criterion to identify regions of nonsmoothness. Such an approach somewhat shares its idea with popular adaptive-mesh-refinement criteria. These criteria are inherently problem dependent, and an optimal design of the troubled cell indicator is at the heart of the DG-FD hybrid method. Requirements on the indicator include

(i) A relatively low computational cost.
(ii) Early and robust detection of spurious oscillations developing on the DG grid.
(iii) Being unflagged as soon as the oscillation no longer exists, so that evolution can be performed by a more efficient DG solver.

Motivated by the idea of the modal shock indicator devised by [98], we adopt the oscillation detection criterion

$$\sqrt{\frac{\sum_i \hat{u}_i^2}{\sum_i u_i^2}}>(N+1-M)^{-\alpha}, \tag{42}$$

where $\hat{u}$ is the solution with the lowest M modes filtered out i.e.

$$\hat{u}(\xi)=\sum_{p=M}^{N}\sum_{q=M}^{N}\sum_{r=M}^{N}c_{p,q,r}L_p(\xi^1)L_q(\xi^2)L_r(\xi^3), \tag{43}$$

and the summations $\sum_i$ in Eq. (42) with the nodal values $u_i, \hat{u}_i$ are performed over all DG grid points. The exponent α in the criterion (42) controls the sensitivity of the indicator. Since we filter out the highest mode on the DG grid, the troubled cell indicator needs to use $M\geq 2$. We use $M=3$ for the troubled cell indicator, effectively monitoring power from the second and third highest modes. Empirically we find that $M\lesssim\lfloor(N+1)/2\rfloor$ provides robust detections of discontinuities without the indicator being excessively triggered. We use $\alpha=4.0$ following Refs. [58,64].

To avoid an element switching back and forth between DG and FD grid in an unnecessarily frequent manner, we

[5]For example, the interpolation scheme between the DG and FD grids does not strictly preserve the force-free conditions or the divergence (Gauss) constraints.

TABLE I. Simulation setup for 1D tests in Sec. IV A. Grid resolution is increased with $n = 0$ (Low), $n = 1$ (Med), and $n = 2$ (High). For the FFE breakdown problem, we use $n = 3$ as a reference solution. Each resolution, if all elements are switched to FD, is equivalent to 352×2^n finite-difference grid points along the x axis.

	Domain size	DG grid points	η	CFL factor	Time step size $(\times 2^{-n})$
Fast wave	$[-0.5, 1.5] \times [-0.1, 0.1]^2$	$(192 \times 2^n) \times 6^2$	10^6	0.3	9.22×10^{-4}
Alfvén wave	$[-1.5, 1.5] \times [-0.1, 0.1]^2$				1.38×10^{-3}
FFE breakdown	$[-0.5, 0.5] \times [-0.1, 0.1]^2$				4.61×10^{-4}

use $\alpha' = \alpha + 1$ when an element is evolving on FD grid. The tighter bound α' ensures an extra smoothness of solution when the grid is switched back to DG, preventing it from switching again to FD within only a few time steps.

Depending on the specific type of an evolved system, one may consider additional physical admissibility criteria (e.g. positivity of the mass density in the case of hydrodynamics) for the troubled cell indicator. Since the only physical constraints in our evolution system, the force-free conditions, are handled by the stiff parallel electric current, we do not impose any physics-motivated criteria.

In our implementation of the DG-FD hybrid scheme for GRFFE, we adopt only one criterion for the troubled cell indicator: application of the modal sensor (42) to the magnitude of $\tilde{B}^i$. While it looks somewhat oversimplified that the information of a single scalar quantity is used for monitoring a system with nine evolution variables $\{\tilde{E}^i, \tilde{B}^i, \tilde{\psi}, \tilde{\phi}, \tilde{q}\}$, we show in Sec. IV that it is capable of detecting troubled elements in a satisfactory manner.

D. Outer boundary condition

In 3D simulations, the outer boundary of the computational domain is usually placed far out to avoid spurious boundary effects leaking into the internal evolution. Still, in order to suppress potential unphysical noise or reflections at the outer boundary, we implement a no-incoming Poynting flux boundary condition as follows. The evolved variables at the outer boundary $\mathbf{U}_{\rm out} = (\tilde{E}^i, \tilde{B}^i, \tilde{\psi}, \tilde{\phi}, \tilde{q})_{\rm out}$ are prescribed as follows. First, we copy the values of $\{\tilde{E}^i, \tilde{B}^i, \tilde{q}\}$ from the outermost grid points. Then, if the Poynting flux is pointing inward, we set $(\tilde{E}^i)_{\rm out}$ to zero. Divergence cleaning scalar fields $(\tilde{\psi})_{\rm out}$ and $(\tilde{\phi})_{\rm out}$ are always set to zero.[6] On the DG grid, $\mathbf{U}_{\rm out}$ is fed as an external state when computing the boundary correction terms. On the FD grid, ghost zones are filled with $\mathbf{U}_{\rm out}$ during the FD reconstruction step.

[6]Normally, the level of errors associated with the divergence cleaning part (ψ, ϕ) is much smaller than that of the physical variables (E^i, B^i, q). Spurious reflections, if any, in the divergence cleaning parts are subdominant to Poynting fluxes transmitting through the outer boundaries.

IV. RESULTS

In this section, we test and assess our implementation of the DG-FD hybrid method for evolving GRFFE equations with a suite of robust code validation problems. We perform 1D tests in Sec. IV A, curved spacetime tests with black holes in Sec. IV B, and pulsar magnetosphere tests in Sec. IV C. We also discuss accuracy and efficiency aspects of the DG-FD hybrid method in Sec. IV D.

A. One-dimensional problems

One-dimensional test problems evolve initial data that only has dependence in the x direction. We use a computational domain consisting of a single element along the y and z axes, and impose periodic boundary condition on those directions. Our lowest grid resolution has 32 elements along the x axis, resulting in 192 DG grid points. To facilitate comparisons with other results available in the literature, we note that this resolution is equivalent to 352 grid points if all elements are switched to an FD grid. The number of elements along the x axis is increased by a factor of two to run medium (64 elements) and high (128 elements) resolutions. Dirichlet boundary conditions are applied at both ends of the x axis. We use the CFL factor 0.3 and parallel conductivity $\eta = 10^6$. Simulation setups are summarized in Table I. Initial conditions for 1D test problems are summarized in Appendix A.

1. Fast wave

Originally due to [40], this test problem evolves a pure fast mode propagating in an electrovacuum. The initial profile advects to the $+x$ direction with the wave speed $\mu = 1$. The analytic solution is $Q(x, t) = Q(x - t, 0)$ for any physical quantity Q.

As shown in Fig. 1, our scheme shows good convergence in flat regions with increasing grid resolution. We observe that the accuracy and numerical convergence of the solution is substantially lost around two kinks present in the initial data (corresponding to $x = 0.5 \pm 0.1$ in Fig. 1) at which spatial derivatives of fields are discontinuous.

2. Alfvén wave

The stationary Alfvén wave problem [24] has a transition layer $|x| < 0.1$ that maintains a strong parallel current, and

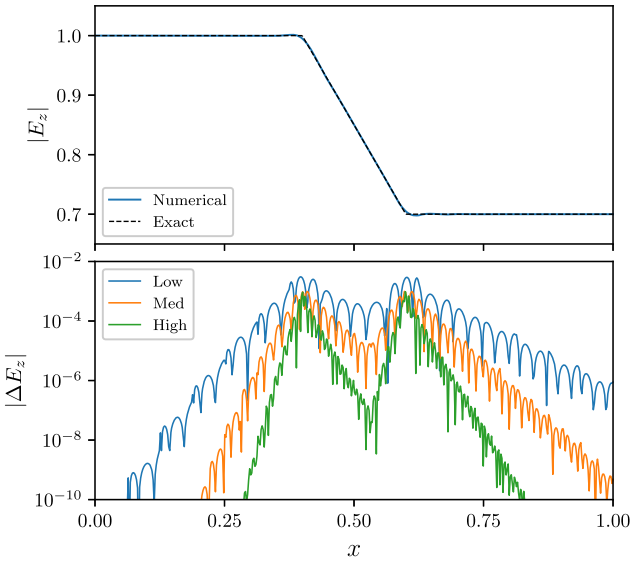

FIG. 1. Fast wave at $t = 0.5$. Top: comparison between the exact solution and a numerical solution with the lowest grid resolution. Bottom: error of E_z for three different grid resolutions.

the accuracy of the test results essentially reflects how well a numerical scheme can maintain the force-free conditions.

We show the result at $t = 2.0$ in Fig. 2. It needs to be noted that time derivatives of fields at $t = 0$, from the initial condition (A2), vanish only if the parallel current $J_i B^i$ equals Eq. (26). In our approach, the region $|x| < 0.1$ initially develops a small transient until the stiff relaxation term becomes fully active within several time steps and effectively recovers the same value of $J_l B^l$. The amplitude of the initial transient rapidly decreases at higher grid resolutions. Owing to the higher-order accuracy of the

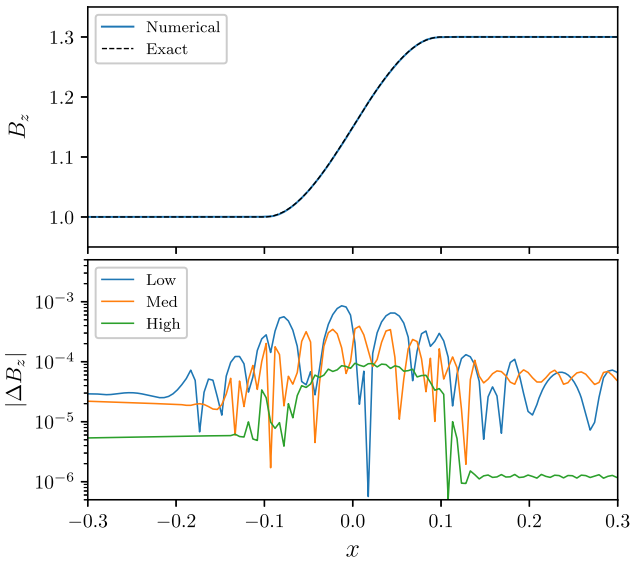

FIG. 2. Stationary Alfvén wave at $t = 2.0$. Same plot description as Fig. 1.

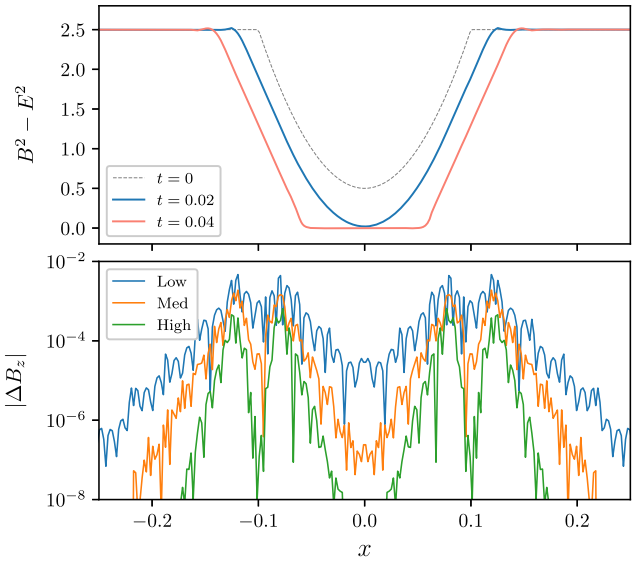

FIG. 3. FFE breakdown problem. Top: initial data ($t = 0$) and a numerical solution with the lowest grid resolution at $t = 0.02$ and $t = 0.04$. Bottom: error of B_z with respect to the reference solution.

discontinuous Galerkin discretization, our result shows good convergence and low amounts of grid dissipation.

3. FFE breakdown

The force-free electrodynamics breakdown problem, originally designed by [40], demonstrates that a state initially satisfying the force-free conditions can later develop into a state violating them. $B^2 - E^2$ decreases over time toward zero in the transition layer $|x| < 0.1$ and the magnetic dominance condition eventually breaks down.

Figure 3 shows numerical results. At $t \gtrsim 0.02$, the rectifier term restoring the $B^2 - E^2 > 0$ condition is switched on and robustly maintains the magnetic dominance at later times. Since this problem does not have a closed form solution, we perform an additional higher resolution run using 256 elements along the x axis and use it as a reference solution to check the convergence. Similar to the fast wave test, we note the loss of accuracy and numerical convergence near the kinks present in the solution.

B. Three-dimensional tests: Black hole magnetospheres

We perform a set of 3D tests in a curved spacetime using black hole magnetosphere problems. The grid structure of the computational domain is portrayed in Fig. 4. A spherical shell spanning the radius $[r_{\rm in}, r_{\rm out}]$ is split into six cubed-sphere wedges, which are then further refined into elements. We use an equiangular coordinate map along angular directions and a logarithmic map along the radial direction.

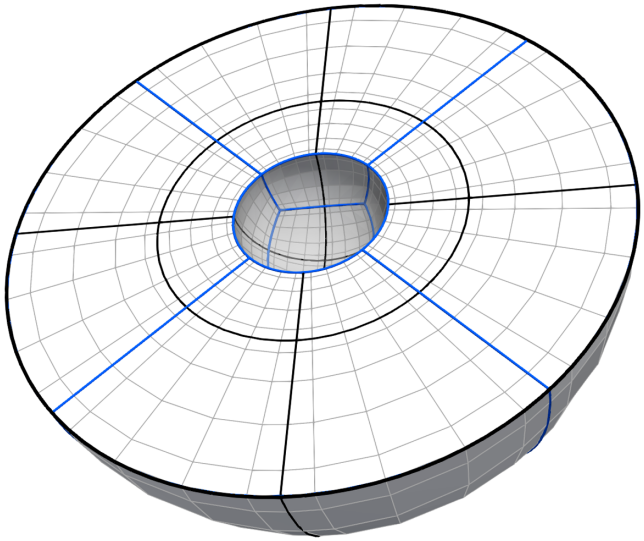

FIG. 4. A half-cut illustration of the spherical grid used for black hole tests in Sec. IV B. Blue lines show boundaries between the cubed-sphere wedges, where black lines show boundaries between each element (in this example, there are 8 elements in each wedge). The DG-P_5 mesh consisting of 6^3 Legendre-Gauss-Lobatto collocation points is shown with gray lines. The total number of elements in this example is $N_r \times N_\Omega = 2 \times 24$.

1. Exact Wald solution

Wald [99] found a stationary electrovacuum solution of Maxwell's equations in the Kerr spacetime. The solution for the 4-potential is given as

$$A_b = \frac{B_0}{2}[(\partial_\phi)_b + 2a(\partial_t)_b], \tag{44}$$

where B_0 is the field amplitude, ∂_t and ∂_ϕ are the Killing vector fields in time and azimuthal directions, and $a = J/M^2$ is the dimensionless spin of the Kerr black hole.

The Wald solution with $a = 0$ satisfies the force-free conditions outside the horizon. Electric and magnetic fields in Kerr-Schild coordinates are given by

$$\begin{aligned}
\tilde{B}^x &= \tilde{B}^y = 0, \\
\tilde{B}^z &= B_0, \\
\tilde{E}^x &= -\frac{2MB_0 y}{r^2}, \\
\tilde{E}^y &= \frac{2MB_0 x}{r^2}, \\
\tilde{E}^z &= 0.
\end{aligned} \tag{45}$$

We evolve the initial condition (45) to $t = 5M$ and measure the L2 error norm

$$L_2(v^i) \equiv \sqrt{\frac{1}{n}\sum_{k=1}^{n}[(v_k^x)^2 + (v_k^y)^2 + (v_k^z)^2]}, \tag{46}$$

where $v^i = \tilde{B}^i_{\text{numerical}} - \tilde{B}^i_{\text{exact}}$ and n is the number of grid points. The inner domain boundary is placed at $r_{\text{in}} = 1.99M$, at which no specific boundary condition is imposed. A Dirichlet boundary condition is imposed at the outer boundary $r_{\text{out}} = 20M$. Conductivity of the magnetosphere is turned off by setting $\eta = 0$.

In Table II, we show convergence studies for different orders of DG schemes $N = 5, 7, 9$. Measured convergence of DG-P_5 and DG-P_7 schemes is consistent with the order of DG discretization. A somewhat slower convergence of the DG-P_9 scheme can be attributed to other limiting factors such as the truncation error from time integration or the sixth-order interpolation from the initial FD grid to DG grid. In all test cases shown in Table II, all elements stayed on the DG grid throughout the evolution.

2. Vacuum Wald problem

A time-dependent evolution of electromagnetic fields around a Kerr black hole can be simulated with the initial magnetic fields given by the Wald solution (44) where electric fields are set to zero at $t = 0$. The system reaches a

TABLE II. Convergence tests of different DG-P_N schemes on the Wald solution (Sec. IV B 1). For each level of grid resolution, we show the number of elements used in radial and angular directions, time step size $\Delta t/M$, L2 error norm of $\tilde{B}^i$ at $t = 5M$, and the measured order of numerical convergence.

	Resolution	Elements ($N_r \times N_\Omega$)	$\Delta t/M$	Error($\tilde{B}^i$)	Convergence order
DG-P_5	Low	1×6	2.90×10^{-2}	8.71×10^{-4}	
	Medium	2×24	1.15×10^{-2}	2.74×10^{-5}	4.99
	High	4×96	5.76×10^{-3}	4.11×10^{-8}	4.72
DG-P_7	Low		1.62×10^{-2}	1.23×10^{-5}	
	Medium		6.29×10^{-3}	1.51×10^{-7}	6.35
	High		3.14×10^{-3}	1.29×10^{-9}	6.87
DG-P_9	Low		1.03×10^{-2}	2.75×10^{-7}	
	Medium		3.95×10^{-3}	2.03×10^{-9}	7.08
	High		1.97×10^{-3}	8.04×10^{-12}	7.98

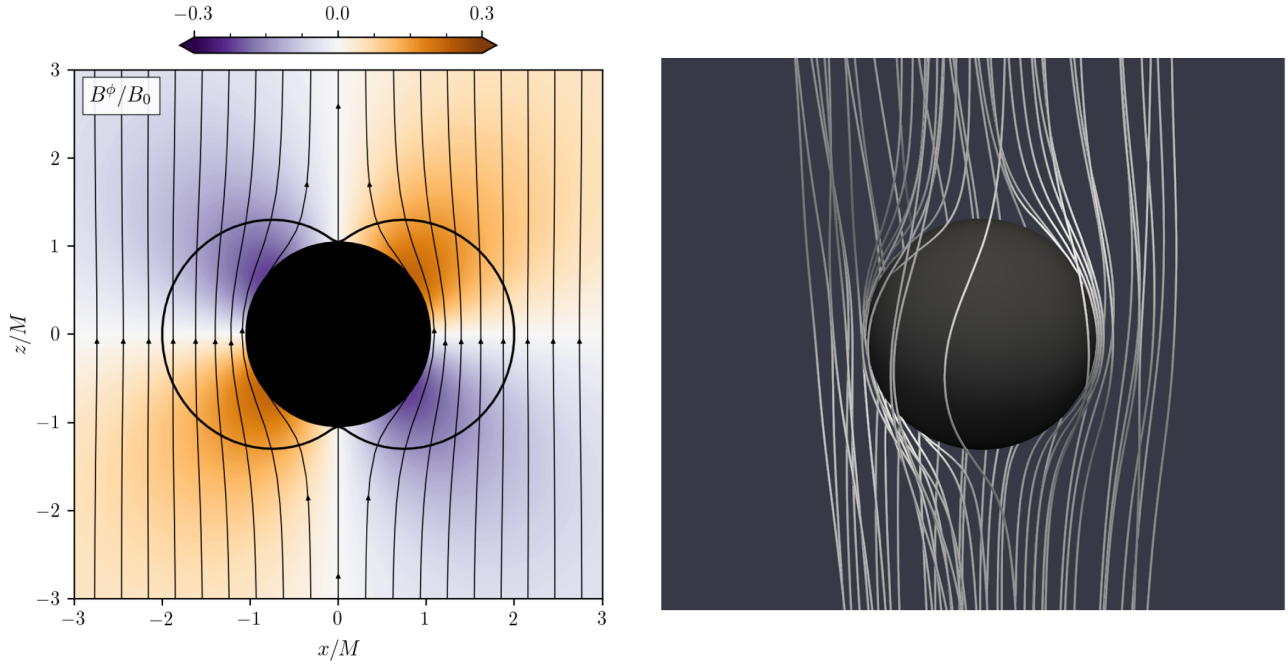

FIG. 5. Vacuum Wald problem (at $t = 125M$) with black hole spin $a = 0.999$. Left: toroidal component of the magnetic field and its in-plane field lines on the meridional plane. We show the interior of the outer horizon $r = r_+$ with a black disk and the ergosphere with black solid lines. Right: a three-dimensional visualization illustrates the magnetic field lines (silver lines) expelled from the horizon (black sphere).

steady state that depends on the spin of the black hole and electrical conductivity of the magnetosphere.

We first simulate the electrovacuum case. The background spacetime is the Kerr metric with $a = 0.999$ in spherical Kerr-Schild coordinates (see Appendices B and C). The electrical conductivity of the magnetosphere is switched off by setting $\eta = 0$. We use $N_r \times N_\Omega = 16 \times 96$ elements and use CFL factor 0.25, resulting in the time step size $\Delta t = 1.97 \times 10^{-3} M$. The inner domain boundary is located at $r_{\rm in} = M$, and the no-incoming Poynting flux boundary condition (see Sec. III D) is applied at the outer domain boundary $r_{\rm out} = 125M$.

The evolution reaches a stationary state after $t \gtrsim 80M$. We show the structure of magnetic fields at $t = 125M$ in Fig. 5. The Kerr black hole expels magnetic field lines, successfully demonstrating the "Meissner effect" of black hole electrodynamics [100].

In a stationary state, total magnetic flux through the upper hemisphere of the outer horizon has an analytic expression [101]

$$\Phi = \oint_{r=r_+, z>0} B^i d\Sigma_i = \pi r_+^2 B_0 \left(1 - \frac{a^4}{r_+^4}\right), \qquad (47)$$

where a is the dimensionless spin of the black hole and $r_+ = M(1 + \sqrt{1 - a^2})$ is the outer horizon radius in spherical Kerr-Schild coordinates. We perform additional simulations varying the black hole spin a using the same grid setup, all reaching stationary states at $t \gtrsim 80M$. We plot the obtained magnetic flux at $t = 125M$ in Fig. 6; our numerical results are in an excellent agreement with the analytic prediction. The troubled cell indicator is flagged at several innermost elements only for the highly spinning cases with $a \geq 0.90$.

3. Magnetospheric Wald problem

First performed by [24], this problem models a highly conductive magnetosphere around a Kerr black hole. The

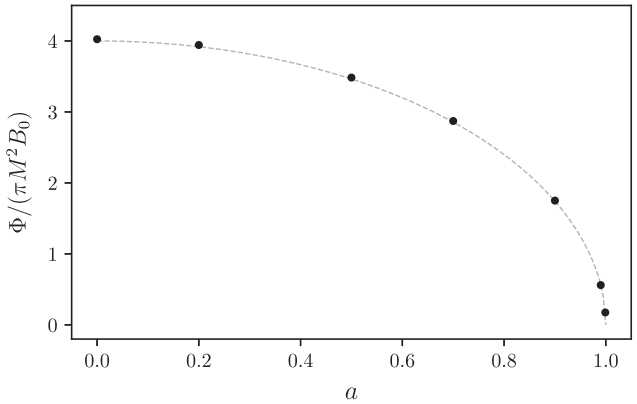

FIG. 6. Vacuum Wald problem: total magnetic flux through the upper hemisphere of the outer horizon versus the spin of the Kerr black hole. Numerical results at $t = 125M$ (black dots) are shown on top of the analytic prediction [dotted line, Eq. (47)].

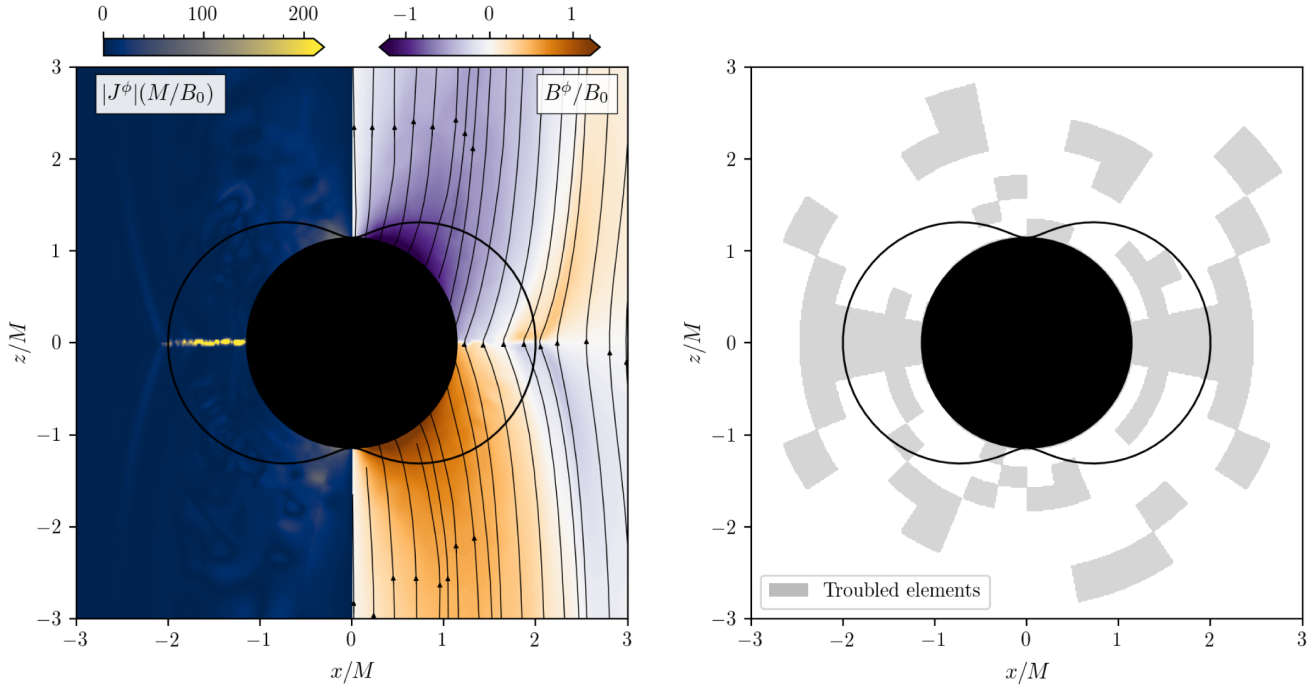

FIG. 7. Magnetospheric Wald problem at $t = 125M$. In both panels, the interior of the outer horizon and the ergosphere are shown with a black disk and a thick black line, respectively. Left: toroidal component of the electric current density and magnetic field. In-plane magnetic field lines are shown with thin black lines in the right half. Right: distribution of troubled elements evolved on the FD grid.

initial condition is the same as the vacuum Wald problem but now the electrical conductivity of the magnetosphere is switched on. Compared to the electrovacuum case, the presence of highly conductive plasma dramatically changes the behavior of the magnetosphere, since the parallel components of electric fields $E_i B^i$ can be neutralized by the parallel electric current. There is no analytic solution to the evolution of this initial value problem, where numerical simulations [e.g. [24,45,46,81,102]] show that the system reaches a quasi-steady state that resembles the analytically derived solutions of a stationary force-free magnetosphere [103].

We perform a test with the black hole spin $a = 0.999$ using $N_r \times N_\Omega = 32 \times 384$ elements with the CFL factor 0.25 ($\Delta t = 9.86 \times 10^{-4} M$). At this grid resolution, if all elements are on the FD grid, there are 176 FD grid points along the θ direction with the minimum radial grid spacing $\Delta r = 0.014M$ at the inner boundary $r = M$. Parallel conductivity is set to $\eta = 10^5 M^{-1}$. Small numerical errors and resulting constraint violations naturally introduce electric charge density into the computational domain via the parallel current Eq. (28), filling up the magnetosphere. The system reaches a stationary state at $t \gtrsim 80M$.

We show the result at $t = 125M$ in Fig. 7. Inside the ergosphere, magnetic field lines are dragged by the rotation of the black hole and a thin current sheet is formed in the equatorial plane. The overall configuration and topology of the magnetic fields agree well with previous results reported in the literature. The troubled cell indicator is always flagged at the elements encompassing the equatorial current sheet, while several more elements sparsely distributed near the ergosphere are also switched to the FD grid (right panel of Fig. 7).

In the high electrical conductivity limit, magnetic field lines entering the ergosphere end up crossing the outer horizon [78,102], apart from a small portion reconnecting at the equatorial current sheet. Because of a large grid resistivity in our setup (the ergosphere is radially ~50 FD grid points across on the equatorial plane), we see that only about half of the magnetic field lines penetrate the horizon. Some temporal variations of the current sheet and magnetic field lines near the ergosphere are observed, but the details of magnetic reconnection and plasmoid formations at the equatorial current sheet [102] are not fully resolved at the current grid resolution.

C. Three-dimensional tests: Pulsar magnetospheres

A conducting sphere threaded with a dipolar magnetic field and rotating in free space serves as a toy model of pulsars. In the flat spacetime, we set the initial dipolar magnetic field as

$$A_\phi = \mu \frac{(x^2 + y^2)}{(r^2 + \delta^2)^{3/2}}, \tag{48}$$

where μ is the magnetic dipole moment, $r^2 = x^2 + y^2 + z^2$, and δ is a small number to regularize the field at $r = 0$. All

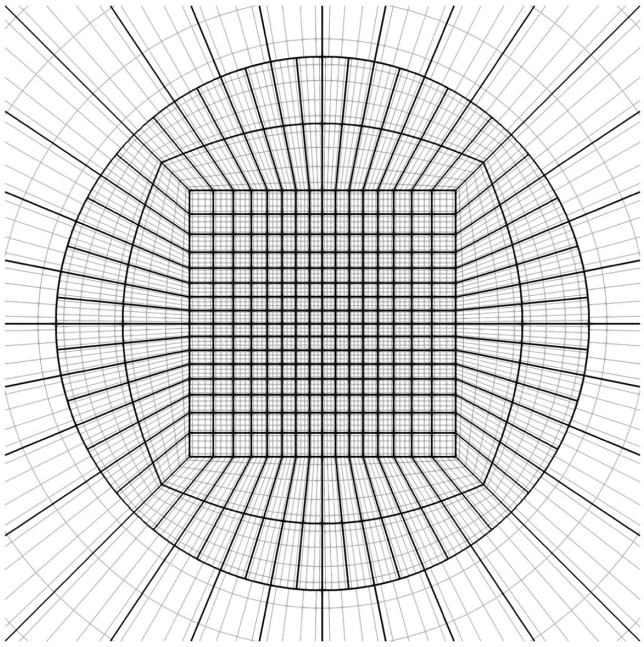

FIG. 8. A zoom-in view of the computational domain used for the pulsar magnetosphere tests in Sec. IV C. A sphere domain is divided into an inner cube at the center, a layer of cubed-sphere wedges, and an outer spherical shell (not fully shown in this figure).

other variables, including electric fields, are set to zero everywhere in the initial data.

Rotation of the star is turned on at $t = 0$ with a fixed angular velocity $\Omega\hat{z}$. Inside the star ($r \leq R$), we enforce the perfect conductor condition

$$E^i + \varepsilon^{ijk}_{(3)} v_j B_k = 0, \tag{49}$$

with the (rigid) rotation velocity field $v^i = \varepsilon^{izj}_{(3)}\Omega x_j$. In practice this is implemented by overwriting electric fields E^i with those consistent with (49) at every substep of time integration. By this means, the magnetic field is effectively anchored and corotates within $r \leq R$, whereas fields at $r > R$ are freely evolved. For consistent behavior of other evolved variables, we also fix $\tilde{\psi} = 0$ and $\tilde{q} = 0$ inside the star. The magnetic part of the evolution equations is freely evolved everywhere. We use $\delta = 0.1R$ for this test.

Denoting the grid refinement level by an integer l, the computational domain consists of an inner cube (2^{3l} elements) and six cubed-sphere wedges ($N_r \times N_\Omega = 2^{l-3} \times 2^{2l}$ elements for each) surrounding it, wrapped with an outer spherical shell $[N_r \times N_\Omega = 2^{l-3} \times (6 \times 2^{2(l-1)})]$. The outer shell uses a logarithmic map along the radial direction and is fixed to stay on the DG grid. Figure 8 shows the grid structure for $l = 4$. The wedges and the outer shell use an equiangular map for the angular directions, leading to nonuniform sizes of the elements in the inner cube: elements closer to the origin have smaller sizes. Vertices of the inner cube are located at $r_{\rm cube} = 10\sqrt{3}R$, and the cubed-sphere wedges fill the region up to $r_{\rm in} = 20R$. The outer shell extends to the outer domain boundary $r_{\rm out} = 60R$, at which the no-incoming Poynting flux boundary condition is imposed. At the $l = 4$ grid resolution, the total number of grid points is $n^{1/3}_{\rm grid} \approx 120$ on the DG grid, and the radius of the rotator R is a single element wide at the center.

We test with the angular velocity $\Omega = (5R)^{-1}$ and use a parallel conductivity $\eta = 10^5 R^{-1}$. Our simulation grid is rotated along the z axis with the same angular speed as the rotator.

1. Aligned rotator

An aligned rotator ($\theta = 0$) is a simple model of a rotating magnetized neutron star with magnetic moment aligned with the axis of rotation. This problem is relatively simple because it is axisymmetric, and has been treated in a large volume of studies (e.g., [25,26,48,50,79,104,105]).

We use the $l = 5$ resolution, which has 22 FD grid points across the rotator radius and $n^{1/3}_{\rm grid} \approx 240$ total grid points across the DG grid, along with the CFL factor 0.25 ($\Delta t = 6.03 \times 10^{-3} R$). Following an initial numerical transient, the magnetosphere of the rotator gradually expands and the system reaches a quasisteady state after one rotation period.

In Fig. 9, we show the distribution of electric charge density and the structure of magnetic fields after two rotation periods ($t = 20\pi R$). Our scheme successfully reproduces all characteristic features of the aligned rotator magnetosphere. An equatorial current sheet is formed outside the light cylinder radius $r_{\rm LC} = \Omega^{-1}$, and magnetic field lines far from the equatorial plane open up to form a monopolelike configuration. Because of the grid resistivity, magnetic field lines $r \gtrsim 2r_{\rm LC}$ spuriously reconnect through the equatorial current sheet. The troubled cell indicator faithfully tracks the current sheet and the regions with rapid variations of the magnetic field, which are likely to develop oscillations on the DG grid, switching elements to the more robust FD grid. The widening of the distribution of the troubled elements is observed in the outer region $r > 10$. While elements near the center of the domain has a cubic shape, the elements in this outer region are deformed (curved) cubes that build up an outer spherical shell (see Fig. 8), and the Jacobian matrix that maps logical and physical coordinates is no longer constant within an element. Ideally, this should have marginal effects on the behavior of the troubled cell indicator, where empirically we find that the indicator becomes slightly more sensitive on the elements with curved shapes.

2. Oblique rotator

Having a misalignment angle between the magnetic moment and the rotation axis, an oblique rotator serves as a more realistic

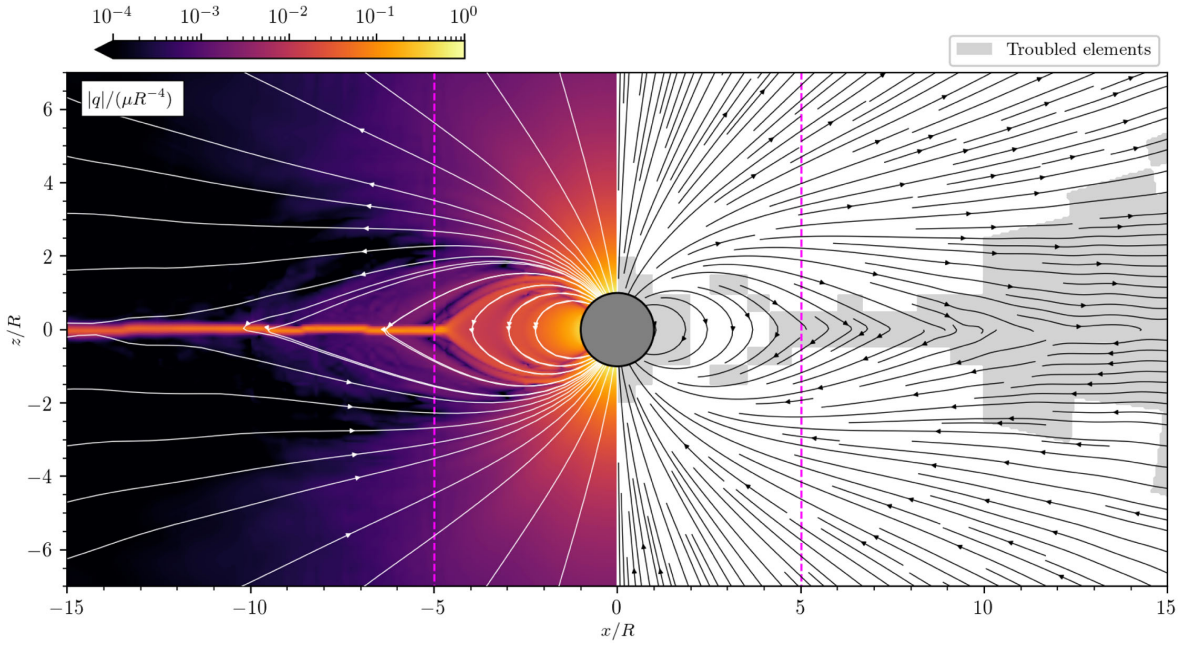

FIG. 9. Aligned rotator after two rotation periods. Magnetic field lines are shown with white solid lines on the left half and black solid lines on the right. Electric charge density is shown with a colormap on the left, and the distribution of troubled elements is shown with gray shades on the right. The light cylinder radius ($r_{\rm LC} = \Omega^{-1}$) is shown with magenta dashed lines.

model of astrophysical pulsars [25,38,49,63,106]. Since the configuration is no longer axisymmetric, a full 3D simulation is required to study this problem.

We use the same simulation setup as the aligned rotator test, but tilt the initial magnetic field by an inclination angle $\theta = \pi/4$. The system reaches a steady state after about one rotation period.

Figure 10 shows simulation snapshots on the equatorial plane (left panel) and meridional plane (right panel) after two periods of rotation. Generic features of the solution are similar to the aligned rotator. Beyond the light cylinder radius, a current sheet is formed and magnetic field lines are opened up. Now that the magnetic axis is misaligned with the rotation axis, the current sheet has a periodically

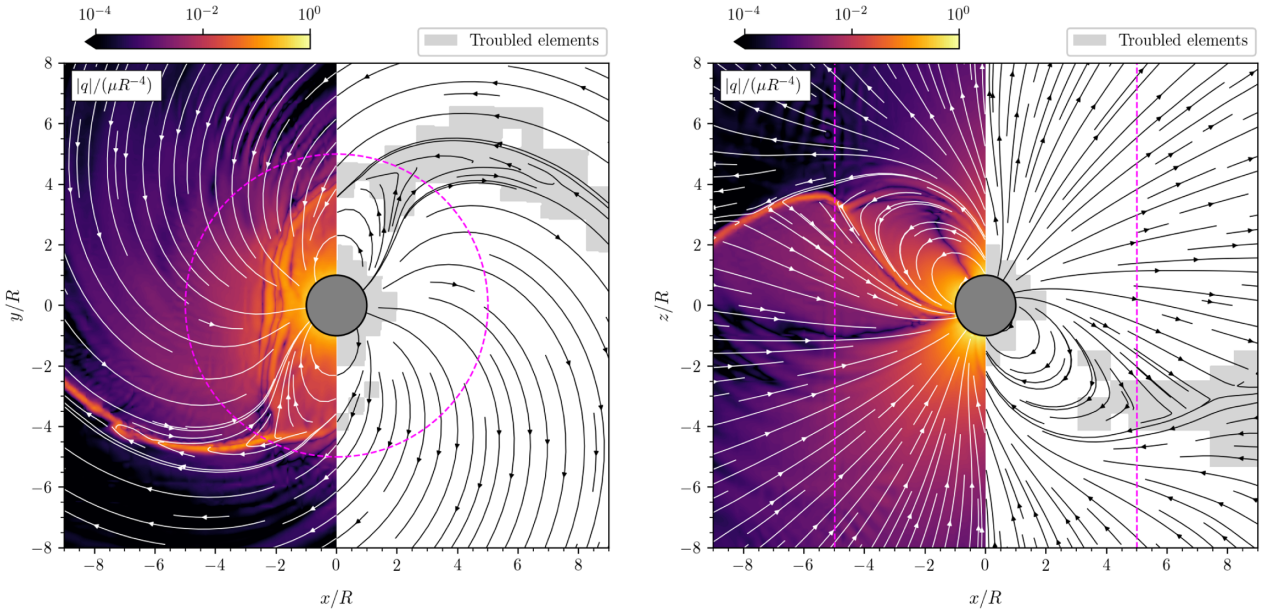

FIG. 10. Oblique rotator: Simulation snapshot on the equatorial (left) and meridional (right) plane after two periods of rotation. Plotted physical quantities and their visualizations are the same as Fig. 9.

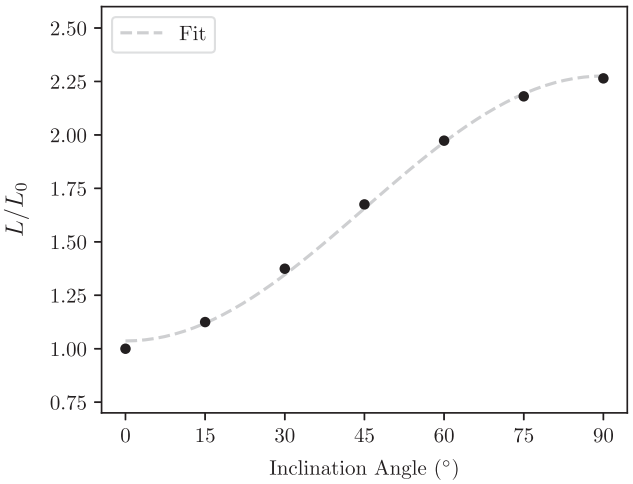

FIG. 11. Oblique rotator: Inclination angle dependence of the spin-down luminosity. Numerical results (black dots) are fitted with the formula (52), shown with a gray dashed line.

modulated curved 3D geometry, appearing as a spiral pattern on the equatorial plane. It is clearly visible that the troubled cell indicator robustly captures and tracks magnetic reconnection points and the spiral current sheet so that the solution can be evolved on the FD grid in those regions. The remainder of the domain keeps evolving on the DG grid, which is computationally more efficient.

One can compute the spin-down luminosity of the rotator

$$L = \oint S_i d\Sigma^i, \tag{50}$$

where

$$S^a = \frac{E^2 + B^2}{2} n^a + \varepsilon^{abc}_{(3)} E_b B_c \tag{51}$$

is the Poynting vector. We perform simulations with a lower grid resolution $l = 4$ for different inclination angles and compute the spin-down luminosity Eq. (50) after two rotation periods at $r = 6R$. Figure 11 shows the measured values. The inclination dependence of the spin-down luminosity L is well fitted with the relation [25]

$$L = L_0(k_1 + k_2 \sin^2\theta) \tag{52}$$

yielding $k_1 = 1.04$ and $k_2 = 1.24$, where L_0 is the luminosity of the aligned configuration ($\theta = 0$).

D. Performance comparison between DG and FD grids

One of the main goals of this work is to assess the performance and cost-saving potential of using a DG-FD hybrid method for global FFE simulations of compact binary magnetospheres. We do so in two steps. First, we establish an accuracy benchmark to identify corresponding DG and FD resolution requirements for the same level of accuracy. Second, using this optimal choice, we estimate the cost-savings/speed-up factor of the DG-FD hybrid methods over traditional FD approaches for the problems presented in this work.

1. Accuracy comparison

Depending on which scheme is taken as the baseline, the DG-FD hybrid method can be interpreted either as a sophisticated shock-capturing technique for the DG method, or an FD method that compresses a group of cells into a high-order spectral representation on smooth regions [58]. The exchange ratio between these two grids, namely $(N+1)^D$ DG grid points and $(2N+1)^D$ FD grid points, has been determined by equalizing the maximum admissible time step sizes [65].

An important follow-up question is comparing the accuracy between the DG and FD grids when the number of grid points is subject to the above ratio. For example, does a compression of 11^3 FD grid points into a P_5 DG mesh with 6^3 grid points in a smooth region lead to an increase or decrease in accuracy? Clearly, the answer is highly dependent on the details of DG (e.g. order of the polynomial, how filtering is applied) and FD solvers (e.g. reconstruction scheme, high-order corrections), which needs to be assessed on a case-by-case basis.

However, it is desirable that the DG and FD solvers have similar levels of accuracy in smooth regions. For instance, coupling a low-order DG scheme with a very high-order FD reconstruction is not ideal since the evolution on the FD grid is computationally too expensive considering the overall achievable accuracy with such a choice. This may possibly make adopting a low-order FD scheme and using an increased number of elements overall more efficient. On the other hand, hybridizing a high-order DG scheme with a low-order FD scheme introduces a relatively large numerical diffusion on the FD grid, artificially smearing out important features, especially on smooth regions close to a discontinuity. In this case, the quality of the solution from the DG-FD hybridization, despite its algorithmic complication, might be no better than simply applying an aggressive DG limiter.

A desired sweet spot is setting the DG and FD discretization to have the same order of convergence. As a fiducial case, we consider the same setup used for the 1D test problems: a DG-P_5 with the highest mode filtered out and a FD solver using the WENO5-Z reconstruction with $q = 2$ along with the fourth-order derivative corrector. Both discretizations are fifth-order convergent for smooth solutions.

We perform a simple numerical experiment as follows. The 1D fast wave problem (see Sec. A) is modified to a smooth initial profile $E_z = -B_y = \sin(2\pi x/\lambda)$ with the wavelength $\lambda = 2$. The computational domain $[0, \lambda]^3$ is split into four elements in each spatial direction. The initial

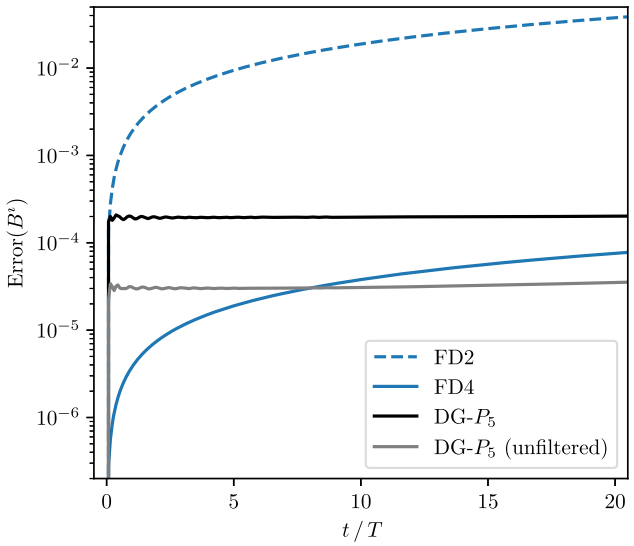

FIG. 12. Error norm of magnetic field over time from a test evolving a sinusoidal fast wave in a periodic box (described in Sec. IV D). For the FD runs, we perform the test without (FD2) and with (FD4) the high-order flux correction.

condition is evolved up to 20 wave crossing times using periodic boundary condition.

Figure 12 shows the time evolution of the error norm of the magnetic field. While both the DG and FD discretizations used in this test have the same fifth-order convergence, the FD grid has a twice smaller grid spacing and shows better accuracy for $t \leq 20\lambda$. We note the boundedness of the error norm on the DG grid, demonstrating a lower numerical dissipation and its resulting suitability for problems involving long-range wave propagation. By contrast, the error norm on the FD grid increases monotonically with time, approaching the same level of error as the DG grid at $t \geq 20\lambda$.

We cautiously interpret this result in the following way. In long-term magnetospheric simulations, replacing the group of $(2N+1)^D$ FD cells with a DG-P_N spectral mesh in smooth regions likely does not harm global accuracy. In simulations with realistic astrophysical scenarios, the solution is not smooth everywhere but will have localized large gradients such as current sheets separated by smooth regions. The global numerical error will then be dominated by the regions with large gradients, since a shock-capturing FD scheme (such as WENO5-Z) will fall back to a lower order.

As an additional example, in Fig. 12 we also show results from an unfiltered DG-P_5 scheme and an FD scheme without the high-order flux correction. The accuracy of the solution on the FD grid is significantly lower without the high-order corrections, the error being even higher than the DG grid using twice fewer grid points per spatial dimension. The unfiltered DG-P_5 has a sixth-order convergence and shows smaller error than the FD grid at $t \gtrsim 10\lambda$. As soon as the DG grid has a higher order of discretization than the order of FD discretization, DG shows a better accuracy in spite of having fewer grid points.

In summary, in particular for the hybridization of a DG-P_5 and a WENO5-Z FD scheme, we conclude that switching from the FD to the DG grid results in a marginal loss of local accuracy in smooth regions, which is unlikely to affect the global error in actual simulations.

2. Efficiency

Having confirmed that the DG and FD grids show a comparable level of accuracy in the setup we use, we now assess potential computational cost savings when using the hybrid scheme. Since the number of grid points on the DG grid is fewer than the FD grid by a factor of $(11/6)^3 = 6.2$ in 3D, a similar amount of computational speedup is naturally anticipated. In order to quantify the actual speedup in our implementation, we run the stationary Alfvén wave test (Sec. IV A 2) using $(N_x, N_y, N_z) = (8, 32, 8)$ elements. We manually force elements to stay on the DG grid for $y > 0$ and on the FD grid for $y < 0$.[7] The fraction of elements running on the FD grid is changed by shifting the upper and lower bounds of the y coordinate. This allows us to vary the fraction of FD to DG grid points in a controlled way. We additionally disable parallelization and carry out all tests in this section on a single CPU core to disentangle parallel scaling from algorithmic performance. Our fiducial benchmark is then given by the overall wall-clock time of the evolution algorithm.

Figure 13 shows the relative speedup compared to the case when all elements are using the FD grid. Since the DG solver does not involve computationally expensive reconstruction steps and has less data communication, it can perform ∼50% more grid point updates per second compared to the FD solver, which results in a combined 9.6× overall speedup. In absolute terms, the measured zone-cycles per CPU second are 108K when all elements are on the DG grid, and 69K when all elements are on the FD grid.

Assuming perfect scaling, the overall speedup relative to the all-FD case can be estimated with the simple formula

$$\frac{1}{x + (1-x)/f} \tag{53}$$

where x is the portion of elements using the FD grid and f is the speedup factor of the DG grid with respect to the FD grid. In Fig. 13, we show the ideal speedup scaling with $f = 9.6$ (gray dashed curve). However, our measurements show that as soon as there is any portion of FD elements,

[7]Therefore, in this controlled experiment, the overhead related to (i) execution of the TCI and (ii) rolling back the time step on troubled elements are excluded. Each element still sends out ghost-zone data to neighboring elements at every time step.

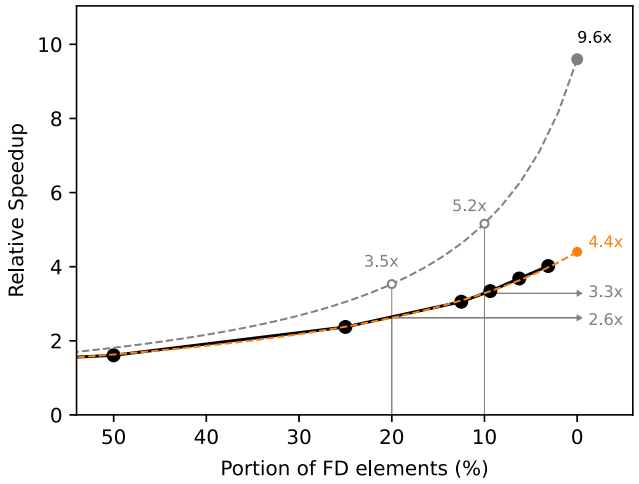

FIG. 13. Single-core wall-clock speedup of the 1D Alfvén wave problem for different fractions of elements using the FD grid. An ideal scaling between all-DG and all-FD is shown with a dashed gray line. The measured scaling (yellow dashed line) fit shows that a DG element runs 4.4× faster on average than an FD element. 10%/20% fraction of FD elements give $3.3\times(5.2\times)/2.6\times(3.5\times)$ overall (ideal) speedup as shown by the solid (dashed) gray line.

the effective speedup factor drops down to $f = 4.4$, implying the presence of an algorithmic bottleneck. When half the elements are using the FD grid, measured zone-cycles per second are 65K, even a bit slower than the all-FD case. This somewhat unexpected drop in performance is likely to be related to an extra interpolation step required at the interface between DG and FD elements to convert the ghost zone data sent between the elements. As a representative number, we quote the achievement of $3.3\times(5.2\times)/2.6\times(3.5\times)$ overall (ideal) speedup when 10% / 20% of elements are using the FD grid.

A separate, detailed profiling of the code suggests at most 10% overhead from the controlling part of the DG-FD hybrid algorithm (applying the TCI to the solution and undoing a time step if an element is troubled), which was excluded in the speedup test described above. Comparing simulations of a smooth wave solution using the DG grid on all elements with the adaptive DG-FD scheme turned on and off showed less than 4% of difference in total runtime.

V. CONCLUSIONS

We have developed a new numerical scheme for general-relativistic FFE based on a DG-FD hybrid method. The numerical scheme combines a high-order spatial discretization with IMEX time stepping to handle stiff source terms associated with maintaining the FFE constraints. We have further implemented a troubled cell indicator capable of flagging spurious features in the DG evolution, allowing the associated elements to transition to a more dissipative conservative FD scheme. In this way, the scheme achieves high-order convergence for smooth problems while robustly tracking and capturing large gradients present in solutions such as current sheets. Our implementation is based on the open-source SpECTRE code and successfully passes and reproduces a suite of standard test problems in one- and three-dimensions. In particular, we achieve up to eighth-order numerical convergence in smooth vacuum problems. A quantitative measure of the numerical resistivity in our scheme, in particular using the approaches by [107,108], will be explored in future works.

In order to assess potential cost savings of this approach over more traditional FD-only schemes, we have performed a quantitative assessment of its accuracy and efficiency. We find that our approach has a potential to speed up FD simulations by the factor of 2–3 with little to no loss of accuracy. We further demonstrate an additional optimization potential of (in some cases) up to a factor 2, when compared to the ideal speed up of the code. Similar or even larger performance gains have been reported when adopting GPU-based parallelization strategies [e.g. [109–111]]. Additional improvements may come from a more optimal set of troubled cell indicator criteria or a dynamic power monitor [e.g. [112]], which can potentially facilitate a more economical grid switching between DG and FD.

The DG-FD hybrid scheme presented here is particularly well suited to study wave propagation as well as accuracy-limited problems, such as steady-state twists or magnetospheric explosion dynamics that evolve on long timescales [e.g. [17,113,114]]. Such studies will be the subject of future work.

ACKNOWLEDGMENTS

The authors are grateful to Kyle Nelli and Nils Vu for helpful discussions and technical support during various stages of this project. Y. K. acknowledges Cristòbal Armaza for encouraging conversations. Computations were performed on the Wheeler cluster and Resnick HPC Center at Caltech. E. R. M. acknowledges support by the National Science Foundation under Grants No. AST-2307394 and No. PHY-2309210, the NSF Frontera supercomputer under grant AST21006, and Delta at the National Center for Supercomputing Applications (NCSA) through allocation No. PHY210074 from the Advanced Cyberinfrastructure Coordination Ecosystem: Services & Support (ACCESS) program, which is supported by National Science Foundation Grants No. 2138259, No. 2138286, No. 2138307, No. 2137603, and No. 2138296. E. R. M. further acknowledges support on Perlmutter through NERSC under Grant No. m4575. The authors acknowledge partial support by the Sherman Fairchild Foundation, and by NSF Grants No. PHY-2207342 and No. OAC-2209655 at Cornell. Figures in this article were produced using Matplotlib [115] and NumPy [116] packages.

APPENDIX A: INITIAL CONDITIONS FOR ONE-DIMENSIONAL PROBLEMS

1. Fast wave

Initial conditions are [40]

$$\begin{aligned} B^x &= 1.0, \\ B^y &= \begin{cases} 1.0 & \text{if } x < -0.1 \\ -1.5x + 0.85 & \text{if } -0.1 < x < 0.1 \\ 0.7 & \text{if } x > 0.1 \end{cases}, \\ B^z &= 0, \\ E^x &= 0, \\ E^y &= 0, \\ E^z &= -B^y. \end{aligned} \tag{A1}$$

2. Stationary Alfvén wave

In the rest frame of the wave, electric and magnetic fields are [24]

$$\begin{aligned} B_x &= 1.0, \\ B_y &= 1.0, \\ B_z &= \begin{cases} 1.0 & \text{if } x < -0.1 \\ 1.15 + 0.15\sin(5\pi x) & \text{if } |x| < 0.1 \\ 1.3 & \text{if } x > 0.1 \end{cases}, \\ E_x &= -B_z, \\ E_y &= 0, \\ E_z &= 1.0. \end{aligned} \tag{A2}$$

The case with nonzero wave speed $-1 < \mu < 1$ can be tested by performing an appropriate Lorentz boost to the initial conditions (A2) [see e.g. [81]].

3. FFE breakdown

The initial state is [40]

$$\begin{aligned} B^x &= 1, \\ B^y = B^z &= \begin{cases} 1 & \text{if } x < -0.1 \\ -10x & \text{if } -0.1 < x < 0.1 \\ -1 & \text{if } x > 0.1 \end{cases}, \\ E^x &= 0, \\ E^y &= 0.5, \\ E^z &= -0.5. \end{aligned} \tag{A3}$$

APPENDIX B: SPHERICAL KERR-SCHILD COORDINATES

The line element of the Kerr spacetime in the Kerr-Schild coordinates is

$$\begin{aligned} ds^2 = &-dt^2 + dx^2 + dy^2 + dz^2 + \frac{2Mr^3}{r^4 + a^2z^2} \\ &\times \left[dt + \frac{r(xdx + ydy) + a(ydx - xdy)}{r^2 + a^2} + \frac{zdz}{r}\right]^2, \end{aligned} \tag{B1}$$

where M is the mass and $a \equiv J/M^2$ is the dimensionless spin of the black hole. The coordinate variable r is defined via the relation

$$\frac{x^2 + y^2}{r^2 + a^2} + \frac{z^2}{r^2} = 1. \tag{B2}$$

For $a = 0$, we see that $r^2 = x^2 + y^2 + z^2$ is the usual radial coordinate used in the spherical coordinate system.

In the spherical Kerr-Schild coordinate system, the Kerr metric has the form

$$\begin{aligned} ds^2 = &-(1 - B)dt^2 + (1 + B)dr^2 + \Sigma d\theta^2 \\ &+ (r^2 + a^2 + Ba^2\sin^2\theta)\sin^2\theta d\phi^2 \\ &+ 2Bdtdr - 2aB\sin^2\theta dtd\phi \\ &- 2a(1 + B)\sin^2\theta drd\phi \end{aligned} \tag{B3}$$

where $\Sigma = r^2 + a^2\cos^2\theta$ and $B = 2Mr/\Sigma$. In the spherical Kerr-Schild coordinates, the inner and outer horizon are located at

$$r_\pm = M(1 \pm \sqrt{1 - a^2}). \tag{B4}$$

The coordinate transformation between the Kerr-Schild coordinates (B1) and the spherical Kerr-Schild coordinates (B3) is

$$x = (r\cos\phi - a\sin\phi)\sin\theta \tag{B5a}$$

$$y = (r\sin\phi + a\cos\phi)\sin\theta \tag{B5b}$$

$$z = r\cos\theta \tag{B5c}$$

APPENDIX C: THE WALD SOLUTION

In the spherical Kerr-Schild coordinates, components of the vector potential (44) are

$$A_t = \frac{B_0}{2}(g_{t\phi} + 2ag_{tt}), \tag{C1a}$$

$$A_r = \frac{B_0}{2}(g_{r\phi} + 2ag_{tr}), \tag{C1b}$$

$$A_\theta = 0, \tag{C1c}$$

$$A_\phi = \frac{B_0}{2}(g_{\phi\phi} + 2ag_{t\phi}). \tag{C1d}$$

Computing magnetic fields from the vector potential C, we get

$$\tilde{B}^r = B_0 r^2 \sin\theta\cos\theta\left[1+\frac{a^2}{r^2}+\frac{2M}{r}\left(\frac{r^4-a^4}{(r^2+a^2\cos^2\theta)^2}-1\right)\right] \tag{C2a}$$

$$\tilde{B}^\theta = -B_0 r\sin^2\theta - \frac{a^2 M B_0 \sin^2\theta}{(r^2+a^2\cos^2\theta)^2}(r^2-a^2\cos^2\theta)(2-\sin^2\theta) \tag{C2b}$$

$$\tilde{B}^\phi = aB_0\sin\theta\cos\theta\left[1+\frac{2Mr(r^2-a^2)}{(r^2+a^2\cos^2\theta)^2}\right]. \tag{C2c}$$

We also write out $\tilde{B}^i$ in the Cartesian representation

$$\bar{x} = r\sin\theta\cos\phi, \tag{C3a}$$

$$\bar{y} = r\sin\theta\sin\phi, \tag{C3b}$$

$$\bar{z} = r\cos\theta, \tag{C3c}$$

which we use for representing tensor quantities in the code. Resulting expressions are

$$\tilde{B}^{\bar{x}} = aB_0\bar{z}\left[(a\bar{x}-r\bar{y})\left\{\frac{1}{r^4}+\frac{2Mr(r^2-a^2)}{(r^4+a^2z^2)^2}\right\}+aMr\bar{x}\left\{\frac{r^2-z^2}{r^4(r^4+a^2z^2)}-\frac{4(r^2+z^2)}{(r^4+a^2z^2)^2}\right\}\right] \tag{C4a}$$

$$\tilde{B}^{\bar{y}} = aB_0\bar{z}\left[(r\bar{x}+a\bar{y})\left\{\frac{1}{r^4}+\frac{2Mr(r^2-a^2)}{(r^4+a^2z^2)^2}\right\}+aMr\bar{y}\left\{\frac{r^2-z^2}{r^4(r^4+a^2z^2)}-\frac{4(r^2+z^2)}{(r^4+a^2z^2)^2}\right\}\right] \tag{C4b}$$

$$\tilde{B}^z = B_0\left[1+\frac{a^2z^2}{r^4}+\frac{Ma^2}{r^3}\left\{1-\frac{z^2(a^2+z^2)(5r^4+a^2z^2)}{(r^4+a^2z^2)^2}\right\}\right]. \tag{C4c}$$

from which one can check that $\tilde{B}^i \to (0,0,B_0)$ for $a \to 0$. We use the expressions (C4) for initializing the densitized magnetic fields $\tilde{B}^i$ in the code.

Note that the barred coordinates $\bar{x}, \bar{y}$ are not equal to the x, y coordinates appearing in the original Kerr-Schild form (B1), whereas $\bar{z} = z$. Barred coordinates $\bar{x}, \bar{y}, \bar{z}$ are simply Cartesian projections of the spherical Kerr-Schild coordinates (B3), where they are related with the Kerr-Schild coordinates by

$$\frac{\bar{x}}{r} = \frac{x}{\sqrt{r^2+a^2}}, \tag{C5a}$$

$$\frac{\bar{y}}{r} = \frac{y}{\sqrt{r^2+a^2}}, \tag{C5b}$$

$$\bar{z} = z, \tag{C5c}$$

$$r^2 = \bar{x}^2+\bar{y}^2+\bar{z}^2. \tag{C5d}$$

[1] C. D. Bochenek, V. Ravi, K. V. Belov, G. Hallinan, J. Kocz, S. R. Kulkarni, and D. L. McKenna, A fast radio burst associated with a Galactic magnetar, Nature (London) **587**, 59 (2020).

[2] Y. Lyubarsky, Fast radio bursts from reconnection in a magnetar magnetosphere, Astrophys. J. **897**, 1 (2020).

[3] J. F. Mahlmann, A. A. Philippov, A. Levinson, A. Spitkovsky, and H. Hakobyan, Electromagnetic fireworks: Fast radio bursts from rapid reconnection in the compressed magnetar wind, Astrophys. J. Lett. **932**, L20 (2022).

[4] C. Thompson and R. C. Duncan, The soft gamma repeaters as very strongly magnetized neutron stars—1. Radiative mechanism for outbursts, Mon. Not. R. Astron. Soc. **275**, 255 (1995).

[5] V. M. Kaspi, F. P. Gavriil, P. M. Woods, J. B. Jensen, M. S. E. Roberts, and D. Chakrabarty, A major soft gamma

repeater-like outburst and rotation glitch in the no-longer-so-anomalous X-ray pulsar 1E 2259 + 586, Astrophys. J. Lett. **588**, L93 (2003).
[6] A. M. Beloborodov, On the mechanism of hard x-ray emission from magnetars, Astrophys. J. **762**, 13 (2013).
[7] R. F. Archibald, V. M. Kaspi, P. Scholz, A. P. Beardmore, N. Gehrels, and J. A. Kennea, Swift observations of two outbursts from the magnetar 4U 0142 + 61, Astrophys. J. **834**, 163 (2017).
[8] M. Tavani *et al.*, An X-ray burst from a magnetar enlightening the mechanism of fast radio bursts, Nat. Astron. **5**, 401 (2021).
[9] A. A. Philippov, B. Cerutti, A. Tchekhovskoy, and A. Spitkovsky, *Ab initio* pulsar magnetosphere: The role of general relativity, Astrophys. J. **815**, L19 (2015).
[10] A. Y. Chen and A. M. Beloborodov, Particle-in-cell simulations of the twisted magnetospheres of magnetars. I, Astrophys. J. **844**, 133 (2017).
[11] T. Uchida, Theory of force-free electromagnetic fields. I. General theory, Phys. Rev. E **56**, 2181 (1997).
[12] A. Gruzinov, Stability in force-free electrodynamics, arXiv:astro-ph/9902288.
[13] A. Tchekhovskoy, A. Spitkovsky, and J. G. Li, Time-dependent 3D magnetohydrodynamic pulsar magnetospheres: Oblique rotators, Mon. Not. R. Astron. Soc. **435**, L1 (2013).
[14] A. Bransgrove, A. M. Beloborodov, and Y. Levin, A quake quenching the Vela pulsar, Astrophys. J. **897**, 173 (2020).
[15] Y. Yuan, A. M. Beloborodov, A. Y. Chen, and Y. Levin, Plasmoid ejection by Alfvén waves and the fast radio bursts from SGR 1935 + 2154, Astrophys. J. Lett. **900**, L21 (2020).
[16] Y. Yuan, A. M. Beloborodov, A. Y. Chen, Y. Levin, E. R. Most, and A. A. Philippov, Magnetar bursts due to Alfvén wave nonlinear breakout, Astrophys. J. **933**, 174 (2022).
[17] K. Parfrey, A. M. Beloborodov, and L. Hui, Dynamics of strongly twisted relativistic magnetospheres, Astrophys. J. **774**, 92 (2013).
[18] J. F. Mahlmann, T. Akgün, J. A. Pons, M. A. Aloy, and P. Cerdá-Durán, Instability of twisted magnetar magnetospheres, Mon. Not. R. Astron. Soc. **490**, 4858 (2019).
[19] F. Carrasco, D. Viganò, C. Palenzuela, and J. A. Pons, Triggering magnetar outbursts in 3D force-free simulations, Mon. Not. R. Astron. Soc. **484**, L124 (2019).
[20] J. F. Mahlmann, A. A. Philippov, V. Mewes, B. Ripperda, E. R. Most, and L. Sironi, Three-dimensional dynamics of strongly twisted magnetar magnetospheres: Kinking flux tubes and global eruptions, Astrophys. J. Lett. **947**, L34 (2023).
[21] L. Lehner, C. Palenzuela, S. L. Liebling, C. Thompson, and C. Hanna, Intense electromagnetic outbursts from collapsing hypermassive neutron stars, Phys. Rev. D **86**, 104035 (2012).
[22] A. Nathanail, E. R. Most, and L. Rezzolla, Gravitational collapse to a Kerr–Newman black hole, Mon. Not. R. Astron. Soc. **469**, L31 (2017).
[23] E. R. Most, A. Nathanail, and L. Rezzolla, Electromagnetic emission from blitzars and its impact on non-repeating fast radio bursts, Astrophys. J. **864**, 117 (2018).
[24] S. S. Komissarov, Electrodynamics of black hole magnetospheres, Mon. Not. R. Astron. Soc. **350**, 427 (2004).
[25] A. Spitkovsky, Time-dependent force-free pulsar magnetospheres: Axisymmetric and oblique rotators, Astrophys. J. **648**, L51 (2006).
[26] J. C. McKinney, Relativistic force-free electrodynamic simulations of neutron star magnetospheres, Mon. Not. R. Astron. Soc. **368**, L30 (2006).
[27] A. Y. Chen, Y. Yuan, and G. Vasilopoulos, A numerical model for the multiwavelength lightcurves of PSR J0030 + 0451, Astrophys. J. Lett. **893**, L38 (2020).
[28] F. Carrasco and M. Shibata, Magnetosphere of an orbiting neutron star, Phys. Rev. D **101**, 063017 (2020).
[29] C. Palenzuela, T. Garrett, L. Lehner, and S. L. Liebling, Magnetospheres of black hole systems in force-free plasma, Phys. Rev. D **82**, 044045 (2010).
[30] C. Palenzuela, L. Lehner, and S. L. Liebling, Dual jets from binary black holes, Science **329**, 927 (2010).
[31] D. Alic, P. Mosta, L. Rezzolla, O. Zanotti, and J. L. Jaramillo, Accurate simulations of binary black-hole mergers in force-free electrodynamics, Astrophys. J. **754**, 36 (2012).
[32] C. Palenzuela, L. Lehner, and S. Yoshida, Understanding possible electromagnetic counterparts to loud gravitational wave events: Binary black hole effects on electromagnetic fields, Phys. Rev. D **81**, 084007 (2010).
[33] F. Carrasco, M. Shibata, and O. Reula, Magnetospheres of black hole-neutron star binaries, Phys. Rev. D **104**, 063004 (2021).
[34] E. R. Most and A. A. Philippov, Electromagnetic precursors to gravitational wave events: Numerical simulations of flaring in pre-merger binary neutron star magnetospheres, Astrophys. J. Lett. **893**, L6 (2020).
[35] E. R. Most and A. A. Philippov, Electromagnetic precursor flares from the late inspiral of neutron star binaries, Mon. Not. R. Astron. Soc. **515**, 2710 (2022).
[36] E. R. Most and A. A. Philippov, Reconnection-powered fast radio transients from coalescing neutron star binaries, Phys. Rev. Lett. **130**, 245201 (2023).
[37] E. R. Most and A. A. Philippov, Electromagnetic precursors to black hole–neutron star gravitational wave events: Flares and reconnection-powered fast radio transients from the late inspiral, Astrophys. J. Lett. **956**, L33 (2023).
[38] C. Kalapotharakos and I. Contopoulos, Three-dimensional numerical simulations of the pulsar magentoshere: Preliminary results, Astron. Astrophys. **496**, 495 (2009).
[39] F. Carrasco and O. Reula, Novel scheme for simulating the force-free equations: Boundary conditions and the evolution of solutions towards stationarity, Phys. Rev. D **96**, 063006 (2017).
[40] S. S. Komissarov, Time-dependent, force-free, degenerate electrodynamics, Mon. Not. R. Astron. Soc. **336**, 759 (2002).
[41] J. Cho, Simulation of relativistic force-free magnetohydrodynamic turbulence, Astrophys. J. **621**, 324 (2005).
[42] E. Asano, T. Uchida, and R. Matsumoto, Time evolution of relativistic force-free fields connecting a neutron star and its disk, Publ. Astron. Soc. Jpn. **57**, 409 (2005).
[43] J. C. McKinney, General relativistic force-free electrodynamics: A new code and applications to black hole

magnetospheres, Mon. Not. R. Astron. Soc. **367**, 1797 (2006).
[44] C. Yu, A high-order WENO-based staggered Godunov-type scheme with constrained transport for force-free electrodynamics, Mon. Not. R. Astron. Soc. **411**, 2461 (2011).
[45] Z. B. Etienne, M.-B. Wan, M. C. Babiuc, S. T. McWilliams, and A. Choudhary, GiRaFFE: An open-source general relativistic force-free electrodynamics code, Classical Quantum Gravity **34**, 215001 (2017).
[46] J. F. Mahlmann, M. A. Aloy, V. Mewes, and P. Cerdá-Durán, Computational general relativistic force-free electrodynamics: I. Multi-coordinate implementation and testing, Astron. Astrophys. **647**, A57 (2021).
[47] A. Dubey, A. Almgren, J. Bell, M. Berzins, S. Brandt, G. Bryan, P. Colella, D. Graves, M. Lijewski, F. Löffler, B. O'Shea, E. Schnetter, B. Van Straalen, and K. Weide, A survey of high level frameworks in block-structured adaptive mesh refinement packages, J. Parallel Distrib. Comput. **74**, 3217 (2014).
[48] K. Parfrey, A. M. Beloborodov, and L. Hui, Introducing PHAEDRA: A new spectral code for simulations of relativistic magnetospheres, Mon. Not. R. Astron. Soc. **423**, 1416 (2012).
[49] J. Petri, The pulsar force-free magnetosphere linked to its striped wind: Time-dependent pseudo-spectral simulations, Mon. Not. R. Astron. Soc. **424**, 605 (2012).
[50] G. Cao, L. Zhang, and S. Sun, Spectral simulations of an axisymmetric force-free pulsar magnetosphere, Mon. Not. R. Astron. Soc. **455**, 4267 (2015).
[51] J. Hesthaven and T. Warburton, *Nodal Discontinuous Galerkin Methods: Algorithms, Analysis, and Applications*, Texts in Applied Mathematics (Springer, New York, 2007).
[52] M. Bugner, T. Dietrich, S. Bernuzzi, A. Weyhausen, and B. Brügmann, Solving 3D relativistic hydrodynamical problems with weighted essentially nonoscillatory discontinuous Galerkin methods, Phys. Rev. D **94**, 084004 (2016).
[53] O. Zanotti, F. Fambri, M. Dumbser, and A. Hidalgo, Space–time adaptive ADER discontinuous Galerkin finite element schemes with *a posteriori* sub-cell finite volume limiting, Comput. Fluids **118**, 204 (2015).
[54] O. Zanotti, F. Fambri, and M. Dumbser, Solving the relativistic magnetohydrodynamics equations with ADER discontinuous Galerkin methods, *a posteriori* subcell limiting and adaptive mesh refinement, Mon. Not. R. Astron. Soc. **452**, 3010 (2015).
[55] F. Fambri, M. Dumbser, S. Köppel, L. Rezzolla, and O. Zanotti, ADER discontinuous Galerkin schemes for general-relativistic ideal magnetohydrodynamics, Mon. Not. R. Astron. Soc. **477**, 4543 (2018).
[56] M. Lombart and G. Laibe, Grain growth for astrophysics with discontinuous Galerkin schemes, Mon. Not. R. Astron. Soc. **501**, 4298 (2020).
[57] A. Reinarz, D. E. Charrier, M. Bader, L. Bovard, M. Dumbser, K. Duru, F. Fambri, A.-A. Gabriel, J.-M. Gallard, S. Köppel, L. Krenz, L. Rannabauer, L. Rezzolla, P. Samfass, M. Tavelli, and T. Weinzierl, Exahype: An engine for parallel dynamically adaptive simulations of wave problems, Comput. Phys. Commun. **254**, 107251 (2020).
[58] N. Deppe *et al.*, Simulating magnetized neutron stars with discontinuous Galerkin methods, Phys. Rev. D **105**, 123031 (2022).
[59] W. Tichy, L. Ji, A. Adhikari, A. Rashti, and M. Pirog, The new discontinuous Galerkin methods based numerical relativity program Nmesh, Classical Quantum Gravity **40**, 025004 (2023).
[60] M. Dumbser, O. Zanotti, E. Gaburro, and I. Peshkov, A well-balanced discontinuous Galerkin method for the first–order Z4 formulation of the Einstein–Euler system, J. Comput. Phys. **504**, 112875 (2024).
[61] M. Cernetic, V. Springel, T. Guillet, and R. Pakmor, Supersonic turbulence simulations with GPU-based high-order discontinuous Galerkin hydrodynamics, arXiv:2401.06841.
[62] J. Pétri, General-relativistic monopole magnetosphere of neutron stars: A pseudo-spectral discontinuous Galerkin approach, Mon. Not. R. Astron. Soc. **447**, 3170 (2015).
[63] J. Petri, General-relativistic force-free pulsar magnetospheres, Mon. Not. R. Astron. Soc. **455**, 3779 (2016).
[64] N. Deppe, F. Hébert, L. E. Kidder, and S. A. Teukolsky, A high-order shock capturing discontinuous Galerkin–finite difference hybrid method for GRMHD, Classical Quantum Gravity **39**, 195001 (2022).
[65] M. Dumbser, O. Zanotti, R. Loubère, and S. Diot, *A posteriori* subcell limiting of the discontinuous Galerkin finite element method for hyperbolic conservation laws, J. Comput. Phys. **278**, 47 (2014).
[66] F. Vilar, *A posteriori* correction of high-order discontinuous Galerkin scheme through subcell finite volume formulation and flux reconstruction, J. Comput. Phys. **387**, 245 (2019).
[67] J. Núñez-de la Rosa and C.-D. Munz, Hybrid DG/FV schemes for magnetohydrodynamics and relativistic hydrodynamics, Comput. Phys. Commun. **222**, 113 (2018).
[68] A. M. Rueda-Ramírez, W. Pazner, and G. J. Gassner, Subcell limiting strategies for discontinuous Galerkin spectral element methods, Comput. Fluids **247**, 105627 (2022).
[69] V. Maltsev, D. Yuan, K. W. Jenkins, M. Skote, and P. Tsoutsanis, Hybrid discontinuous Galerkin-finite volume techniques for compressible flows on unstructured meshes, J. Comput. Phys. **473**, 111755 (2023).
[70] I. Legred, Y. Kim, N. Deppe, K. Chatziioannou, F. Foucart, F. Hébert, and L. E. Kidder, Simulating neutron stars with a flexible enthalpy-based equation of state parametrization in SpECTRE, Phys. Rev. D **107**, 123017 (2023).
[71] L. Pareschi and G. Russo, Implicit–explicit Runge–Kutta schemes and applications to hyperbolic systems with relaxation, J. Sci. Comput. **25**, 129 (2005).
[72] C. W. Misner, K. S. Thorne, and J. A. Wheeler, *Gravitation* (W. H. Freeman, San Francisco, 1973).
[73] C. Palenzuela, Modelling magnetized neutron stars using resistive magnetohydrodynamics, Mon. Not. R. Astron. Soc. **431**, 1853 (2013).
[74] A. Schoepe, D. Hilditch, and M. Bugner, Revisiting hyperbolicity of relativistic fluids, Phys. Rev. D **97**, 123009 (2018).

[75] D. Hilditch and A. Schoepe, Hyperbolicity of divergence cleaning and vector potential formulations of general relativistic magnetohydrodynamics, Phys. Rev. D **99**, 104034 (2019).
[76] C. R. Evans and J. F. Hawley, Simulation of magnetohydrodynamic flows: A constrained transport model, Astrophys. J. **332**, 659 (1988).
[77] A. Dedner, F. Kemm, D. Kröner, C. D. Munz, T. Schnitzer, and M. Wesenberg, Hyperbolic divergence cleaning for the MHD equations, J. Comput. Phys. **175**, 645 (2002).
[78] S. S. Komissarov, Multidimensional numerical scheme for resistive relativistic magnetohydrodynamics, Mon. Not. R. Astron. Soc. **382**, 995 (2007).
[79] P. Goldreich and W. H. Julian, Pulsar electrodynamics, Astrophys. J. **157**, 869 (1969).
[80] H. P. Pfeiffer and A. I. MacFadyen, Hyperbolicity of force-free electrodynamics, arXiv:1307.7782.
[81] V. Paschalidis and S. L. Shapiro, A new scheme for matching general relativistic ideal magnetohydrodynamics to its force-free limit, Phys. Rev. D **88**, 104031 (2013).
[82] P. Moesta, D. Alic, L. Rezzolla, O. Zanotti, and C. Palenzuela, On the detectability of dual jets from binary black holes, Astrophys. J. Lett. **749**, L32 (2012).
[83] B. Cerutti, A. Philippov, K. Parfrey, and A. Spitkovsky, Particle acceleration in axisymmetric pulsar current sheets, Mon. Not. R. Astron. Soc. **448**, 606 (2015).
[84] N. Deppe, W. Throwe, L. E. Kidder, N. L. Vu, K. C. Nelli, C. Armaza, M. S. Bonilla, F. Hébert, Y. Kim, P. Kumar, G. Lovelace, A. Macedo, J. Moxon, E. O'Shea, H. P. Pfeiffer, M. A. Scheel, S. A. Teukolsky, N. A. Wittek *et al.*, SpECTRE v2024.02.05, 10.5281/zenodo.10619885 (2024).
[85] D. A. Kopriva, *Implementing Spectral Methods for Partial Differential Equations* (Springer, Dordrecht, 2009).
[86] S. A. Teukolsky, Formulation of discontinuous Galerkin methods for relativistic astrophysics, J. Comput. Phys. **312**, 333 (2016).
[87] S. A. Teukolsky, Short note on the mass matrix for Gauss–Lobatto grid points, J. Comput. Phys. **283**, 408 (2015).
[88] B. Cockburn and C.-W. Shu, Runge–Kutta discontinuous Galerkin methods for convection-dominated problems, J. Sci. Comput. **16**, 173 (2001).
[89] E. Hairer, S. Nørsett, and G. Wanner, *Solving Ordinary Differential Equations II: Stiff and Differential-Algebraic Problems* (Springer, New York, 1993).
[90] C.-W. Shu and S. Osher, Efficient implementation of essentially non-oscillatory shock-capturing schemes, J. Comput. Phys. **77**, 439 (1988).
[91] C.-W. Shu and S. Osher, Efficient implementation of essentially non-oscillatory shock-capturing schemes, II, J. Comput. Phys. **83**, 32 (1989).
[92] L. Del Zanna, O. Zanotti, N. Bucciantini, and P. Londrillo, ECHO: A Eulerian conservative high-order scheme for general relativistic magnetohydrodynamics and magnetodynamics, Astron. Astrophys. **473**, 11 (2007).
[93] E. R. Most, L. J. Papenfort, and L. Rezzolla, Beyond second-order convergence in simulations of magnetized binary neutron stars with realistic microphysics, Mon. Not. R. Astron. Soc. **490**, 3588 (2019).
[94] V. Rusanov, The calculation of the interaction of non-stationary shock waves and obstacles, USSR Comput. Math. Math. Phys. **1**, 304 (1962).
[95] T. Nonomura and K. Fujii, Robust explicit formulation of weighted compact nonlinear scheme, Comput. Fluids **85**, 8 (2013).
[96] Y. Chen, G. Tóth, and T. I. Gombosi, A fifth-order finite difference scheme for hyperbolic equations on block-adaptive curvilinear grids, J. Comput. Phys. **305**, 604 (2016).
[97] R. Borges, M. Carmona, B. Costa, and W. S. Don, An improved weighted essentially non-oscillatory scheme for hyperbolic conservation laws, J. Comput. Phys. **227**, 3191 (2008).
[98] P.-O. Persson and J. Peraire, Sub-cell shock capturing for discontinuous Galerkin methods, in *44th AIAA Aerospace Sciences Meeting and Exhibit*, 10.2514/6.2006-112.
[99] R. M. Wald, Black hole in a uniform magnetic field, Phys. Rev. D **10**, 1680 (1974).
[100] S. S. Komissarov and J. C. McKinney, Meissner effect and Blandford-Znajek mechanism in conductive black hole magnetospheres, Mon. Not. R. Astron. Soc. **377**, L49 (2007).
[101] A. R. King, J. P. Lasota, and W. Kundt, Black holes and magnetic fields, Phys. Rev. D **12**, 3037 (1975).
[102] K. Parfrey, A. Philippov, and B. Cerutti, First-principles plasma simulations of black-hole jet launching, Phys. Rev. Lett. **122**, 035101 (2019).
[103] A. Nathanail and I. Contopoulos, Black hole magnetospheres, Astrophys. J. **788**, 186 (2014).
[104] I. Contopoulos, D. Kazanas, and C. Fendt, The axisymmetric pulsar magnetosphere, Astrophys. J. **511**, 351 (1999).
[105] S. S. Komissarov, Simulations of the axisymmetric magnetospheres of neutron stars, Mon. Not. R. Astron. Soc. **367**, 19 (2006).
[106] F. Carrasco, C. Palenzuela, and O. Reula, Pulsar magnetospheres in general relativity, Phys. Rev. D **98**, 023010 (2018).
[107] T. Rembiasz, M. Obergaulinger, P. Cerdá-Durán, M.-Á. Aloy, and E. Müller, On the measurements of numerical viscosity and resistivity in Eulerian MHD codes, Astrophys. J. Suppl. Ser. **230**, 18 (2017).
[108] J. F. Mahlmann, M. A. Aloy, V. Mewes, and P. Cerdá-Durán, Computational general relativistic force-free electrodynamics: II. Characterization of numerical diffusivity, Astron. Astrophys. **647**, A58 (2021).
[109] M. T. P. Liska, K. Chatterjee, D. Issa, D. Yoon, N. Kaaz, A. Tchekhovskoy, D. van Eijnatten, G. Musoke, C. Hesp, V. Rohoza, S. Markoff, A. Ingram, and M. van der Klis, H-AMR: A new GPU-accelerated GRMHD code for exascale computing with 3d adaptive mesh refinement and local adaptive time stepping, Astrophys. J. Suppl. Ser. **263**, 26 (2022).
[110] L. Del Zanna, S. Landi, L. Serafini, M. Bugli, and E. Papini, A GPU-accelerated modern Fortran version of the ECHO code for relativistic magnetohydrodynamics, Fluids **9**, 16 (2024).

[111] P. Grete, F. W. Glines, and B. W. O'Shea, K-Athena: A performance portable structured grid finite volume magnetohydrodynamics code, IEEE Trans. Parallel Distrib. Syst. **32**, 85 (2021).
[112] B. Szilágyi, Key elements of robustness in binary black hole evolutions using spectral methods, Int. J. Mod. Phys. D **23**, 1430014 (2014).
[113] Y. Yuan, A. Spitkovsky, R. D. Blandford, and D. R. Wilkins, Black hole magnetosphere with small-scale flux tubes—II. Stability and dynamics, Mon. Not. R. Astron. Soc. **487**, 4114 (2019).
[114] Y. Yuan, Y. Levin, A. Bransgrove, and A. Philippov, Alfvén wave mode conversion in pulsar magnetospheres, Astrophys. J. **908**, 176 (2021).
[115] T. A. Caswell *et al.*, Matplotlib/Matplotlib: Rel: v3.7.1 (2023), https://zenodo.org/records/7697899.
[116] C. R. Harris *et al.*, Array programming with NumPy, Nature (London) **585**, 357 (2020).